Chemical Geology 559 (2021) 119886

Contents lists available at ScienceDirect

Chemical Geology

journal homepage: www.elsevier.com/locate/chemgeo

Experimental weathering of a volcaniclastic critical zone profile: Key role of colloidal constituents in aqueous geochemical response

B.G. Moravec[a], V. Keifer[b], R.A. Root[a], A.M. White[c], Y. Wang[a], Y. Olshansky[a,d], J. McIntosh[c], J. Chorover[a,*]

[a] *Department of Environmental Science, University of Arizona, 1177 E. 4th Street, Tucson, AZ 85721-0038, USA*
[b] *Department of Biology, Bates College, 44 Campus Avenue, Lewiston, ME 04240, USA*
[c] *Department of Hydrology and Atmospheric Sciences, University of Arizona, 1133 E. James E. Rogers Way, Tucson, AZ 85721-0011, USA*
[d] *Department of Crop, Soil and Environmental Sciences, Auburn University, 201 Funchess Hall, Auburn, AL 36849, USA*

ARTICLE INFO

Editor: Oleg Pokrovsky

Keywords:
Mineral transformation
Q-XRD
D-XRD
Colloidal dispersion
Extrusive igneous regolith
Batch dissolution kinetics
Critical zone profile

ABSTRACT

Weathering profiles are often complex, extending from more highly transformed materials in the near surface (e.g., mobile soils) to less weathered parent material (e.g., variably porous bedrock) at depth. It is difficult to resolve from field data the impacts of material properties on the short-term rates of mineral weathering when different depths of the profile are reacted with aggressive meteoric waters (i.e., dilute and undersaturated with respect to primary silicates). In the present study, we aimed to measure variation in mineral transformation reactions that occurs under controlled laboratory conditions for samples collected as a function of depth (e.g., spatial distribution of geologic texture, mineral assemblage, and weathering features) across a deep weathering profile in volcaniclastic parent rock. We conducted a series of batch weathering experiments of extracted core materials from two borings to 35 m across a zero-order catchment in the rhyolitic Jemez River Basin Critical Zone Observatory, NM, USA. Upon reaction with aqueous solutions pre-equilibrated with atmospheric CO_2, mineral dissolution was not limited to one phase, but included a combination of reactions including (at decreasing weathering rates) calcite > zeolites > phyllosilicates > amorphous SiO_2 > feldspar. Mineral transformation rates were dependent on the mineral assemblage, texture, and legacy of hydrothermal alteration. Results also indicated an important role of existing and neoformed colloids in Al, Si, and Fe mobilization and redistribution, especially for materials with evidence of previous hydrothermal alteration. Volcanic breccia, which makes up the top 14 m of the western portion of the catchment, was comprised primarily of weathered lithics, where aqueous solution chemistry was controlled by rapid calcite dissolution/precipitation reactions. Hydrothermally altered tuff, which makes up the top 15 m over most of the catchment, exhibited initial dispersion of colloidal zeolites, which subsequently dissolved, giving rise to smectite precipitation (either in-situ and/or along flowpaths). Solute signatures deriving from water/rock interactions in deep, hydrothermally-altered vesicular tuff were comparable to those in shallow altered tuff, but different from those in deep, unaltered, fracture-dominated tuff. We attribute differences to reactive surface area susceptible to chemical attack by aggressive waters (greater in altered rocks) and primary mineral shielding by Fe and Mn oxides on fracture surfaces in unaltered tuff. This study highlights the use of experimental weathering of extracted cores to help interpret field-based, hydrochemistry with an approach that may be employed in other geologically complex terrains.

1. Introduction

Critical zone (CZ) weathering profiles typically reveal more weathered material, and a predominance of secondary mineral assemblages, in the near surface with gradual transitions to less weathered material, dominated by primary mineral assemblages directly inherited from bedrock at depth. Subsurface CZ architecture consists of gradients in mineralogy, geochemical composition, specific surface area, and porosity as a function of depth, which vary across climate and lithology (Holbrook et al., 2019; Jin et al., 2010; Navarre-Sitchler et al., 2015; Rasmussen et al., 2011). Understanding how these gradients in solid phase composition and architecture affect the chemistry of pore water

---

* Corresponding author.
E-mail address: chorover@arizona.edu (J. Chorover).

https://doi.org/10.1016/j.chemgeo.2020.119886
Received 1 July 2020; Received in revised form 4 September 2020; Accepted 10 September 2020

during its migration through the CZ has been the focus of field efforts (Hoagland et al., 2017; Hunsaker and Johnson, 2017; Kim et al., 2017; Olshansky et al., 2018; White et al., 2019) and reactive transport models (Bao et al., 2017; Ibarra et al., 2016; Li et al., 2017). Still, fundamental questions remain, including: *What are the incongruent mineral transformation reactions occurring along flowpaths at different depths in critical zone profiles that are comprised of complex mineral assemblages? How do these reactions contribute to the evolution of pore water chemistry? How does the evolving pore water chemistry feedback to affect reactions at the mineral-water interface?*

Numerous studies have sought to measure controlling weathering reactions and rates in situ and ex situ, including laboratory experiments for both specimen minerals and naturally occurring mineral assemblages (Barker et al., 1998; Berg and Banwart, 2000; Brantley and Olsen, 2014; Casey and Bunker, 1990; Lee et al., 1998; Malmström et al., 2000; Navarre-Sitchler and Brantley, 2007; White and Buss, 2013). It is well known that laboratory determined weathering rates are generally higher than those measured in the field due to the abrasion of particles, exposure of surfaces to chemical attack that would otherwise be protected in-situ by lithologic and diagenetic structure, and reaction with aqueous solutions of low relative mineral saturation state (e.g., Brantley and White, 2009; Casey et al., 1993; van Grinsven and van Riemsdijk, 1992). However, laboratory studies of weathering reactions in natural geologic materials have the potential to provide useful insights into how variations across weathering profiles control pore water chemistry and local mineral transformations (e.g., Casey et al., 1993). Experimental determination of weathering has rarely been done for deep weathering profiles where mineral composition changes with depth across the CZ.

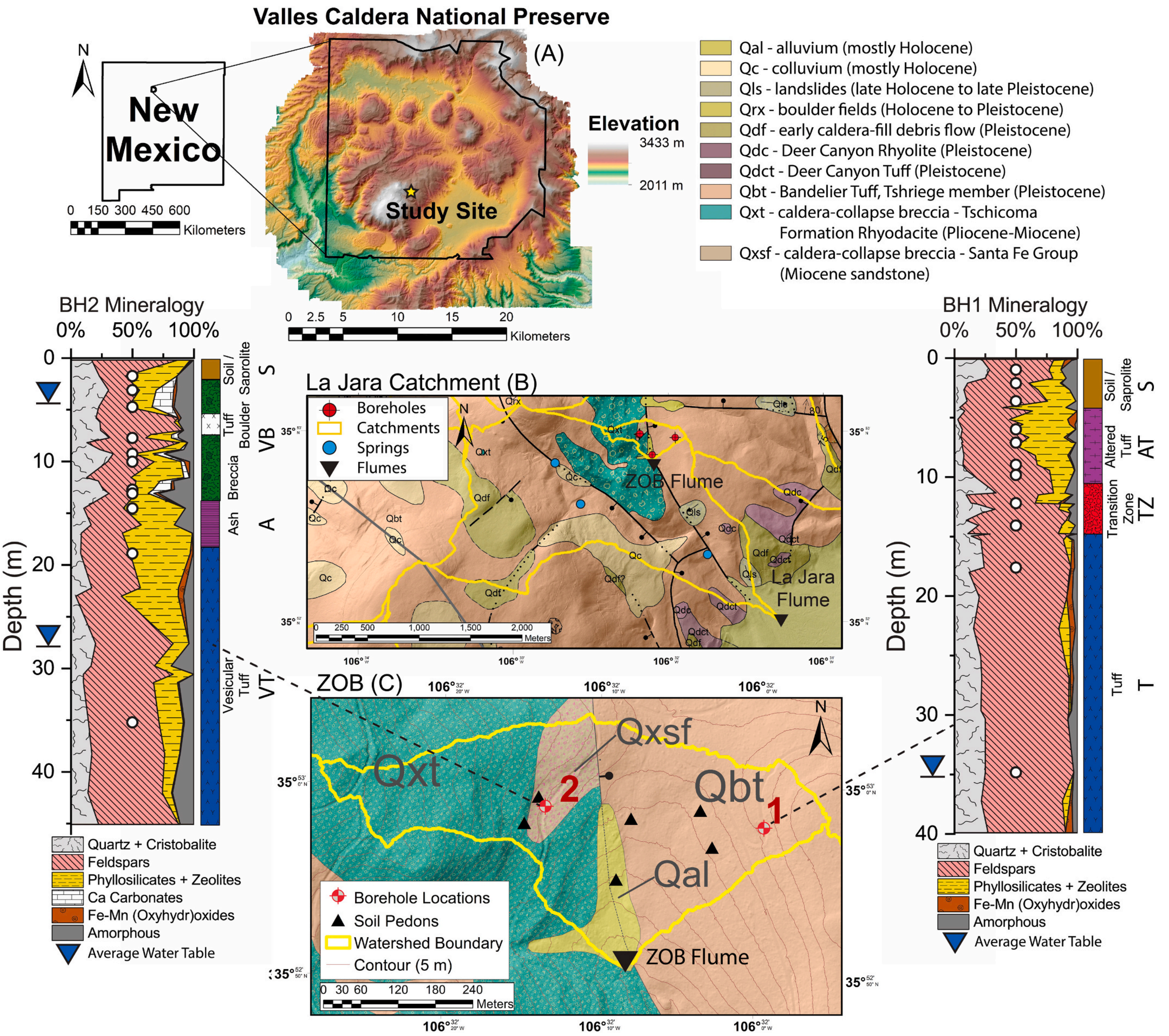

Fig. 1. Site locations in the Jemez River Basin critical zone observatory (CZO), Valles Caldera National Preserve, northern NM, USA (A), La Jara catchment (B), and zero-order basin (ZOB, C). Explanation of geologic units provided for panels (B) and (C) (modified from Goff et al., 2011). Extracted cores were retrieved during the summer of 2016 at boreholes 1 and 2 (BH1 and BH2, respectively). Quantitative mineral composition with depth for BH1 and BH2 are provided for reference along with abbreviations for interpreted units (BH1: T = tuff, TZ = transition zone, AT = altered tuff, and S = soil/saprolite; BH2: VT = vesicular tuff, A = ash, VB = volcanic breccia, S = soil/saprolite); dots on mineral profiles show depths of samples used for this study (modified from Moravec et al., 2020). Average water table depths are shown on profiles, with a perched water table shown in BH2.

Documenting the nature of incongruent weathering reactions as a function of profile depth and water-rock contact time augments our understanding of solute sources and secondary precipitates encountered along hydrologic flowpaths (Brantley and White, 2009). Lab-based weathering rates can then be evaluated in the context of field observations, which includes a clear understanding of the spatial heterogeneity of subsurface architecture, to improve our understanding of preferential flowpaths, water residence times, and characteristics and distribution of the fluid-surface interface.

Ongoing work in the complex volcanic setting of the Jemez River Basin Critical Zone Observatory (JRB-CZO) located in the Valles Caldera National Preserve (VCNP), NM, USA (Fig. 1) seeks to conceptualize the evolution of aqueous geochemistry along hydrologic flowpaths by integrating distributed and nested sampling locations (e.g., precipitation, soil solution, vadose zone, groundwater, and stream water) with an iteratively improved understanding of hydrologic response (McIntosh et al., 2017; Olshansky et al., 2018; Vazquez-Ortega et al., 2015; White et al., 2019; Zapata-Rios et al., 2015). Importantly, headwater catchments in alpine/subalpine environments (such as the headwater catchments of the JRB-CZO) play important roles in water resource availability down gradient (e.g., McGlynn et al., 2004), and they serve as a bellwether for alterations in water quality and quantity in larger stream and river networks due to land-use and climate change (e.g., Ockenden et al., 2016). Like many alpine/subalpine hydrologic systems (e.g., Beria et al., 2017; Cochand et al., 2019; Jenicek and Ledvinka, 2020; Tague and Grant, 2009), deep groundwater recharge in the JRB-CZO primarily occurs during snowmelt in early spring coupled with solute export to surface water driven by the snowmelt fluxes (McIntosh et al., 2017; Olshansky et al., 2018; White et al., 2019; Zapata-Rios et al., 2015).

However, groundwater response to infiltration varies depending on surface morphology and subsurface architecture. For example, in an intensively studied zero order basin in the JRB-CZO, borehole 1 (BH1, Fig. 1) exhibits a flashy response to snowmelt, reflecting flow through dominantly fractured bedrock, whereas borehole 2 (BH2, Fig. 1) exhibits a muted response, reflecting matrix dominated hydrology (White et al., 2019). This deep CZ heterogeneity contributes to a dynamic hydrologic setting where water table elevations and stream discharge respond differently to inputs over relatively short distances, giving rise to a convoluted hydrochemistry of surface waters (White et al., 2019). Moreover, surface water discharge during snowmelt consists of a complex solution chemistry deriving from multiple processes including biologically-induced weathering, metal- and nutrient-ligand transport, groundwater throughflow, and colloid mobilization whose concentration-discharge relationships depend on distributed catchment sources and timing within the snowmelt hydrograph (Olshansky et al., 2018; Vazquez-Ortega et al., 2015).

Field-based concentration-discharge observations have raised several new questions, including the mechanisms underlying differences in solute and colloid export timing (e.g., decoupling of Na and Si release to shallow groundwater in response to snowmelt), the nature and source of colloids, upgradient locations contributing to deep groundwater chemistry, and subsurface architectural controls over spatial distributions in solute chemistry (e.g., Olshansky et al., 2018; Trostle et al., 2016). Coring and analysis of three catchment locations to 46 m (Moravec et al., 2020) revealed a highly complex CZ weathering profile that varies laterally as well as with depth, comprising volcanic glass, feldspars, weathered lithics, zeolites, and secondary phyllosilicates (Fig. 1, only BH1 and BH2 shown). Moravec et al. (2020) dissected the weathering profiles into discrete zones using discriminant statistical analysis of complimentary geophysical, mineralogical, and bulk chemical datasets and proposed historic weathering trajectories that formed the CZ architecture as it exists today. The combined results of these prior studies show that the geochemical, mineralogical, and structural heterogeneity of the weathering profile (in the vertical and horizontal domains) contributes significantly to the spatiotemporal complexity of vadose zone, groundwater and surface water solutions. We contend that when coupled with intensive field monitoring, laboratory-based weathering of material from intact cores should provide novel insights into the specific incongruent dissolution reactions occurring in the field site as a function of depth, including their combined effects on water chemistry. Doing so should help us to develop mechanistic relationships for observed spatiotemporal variability in water chemistry observed at the site.

We hypothesized that the previously identified weathering profile zones (Moravec et al., 2020) contribute distinct aqueous geochemical signatures through interactions with contrasting mineral constituents, and we sought to test this under controlled experimental conditions. A series of lab-based, batch weathering experiments were performed on extracted core materials (down to 35 m, Fig. 1) for time points from 1 h to 1 y. We report here on weathering rates, mineral compositional changes, colloid composition, and resulting solute chemistry of reacted lithologic materials, which provide contextual data complementary to field-based water chemistry previously published for this site (McIntosh et al., 2017; Olshansky et al., 2018; White et al., 2019; Zapata-Rios et al., 2015).

2. Methods

2.1. Site description

Drill-core samples (BH1 and BH2) used for this study were extracted from two locations within a highly-instrumented 16 ha zero-order basin (ZOB) in the VCNP in north central New Mexico, USA (Fig. 1) (Lat: 35.8825°, Long: −106.5353°) (Moravec et al., 2020). The ZOB is a headwater sub-catchment within the larger La Jara drainage of the JRB-CZO (Brooks and Vivoni, 2008; Chorover et al., 2011). It is located on the northwest flank of Redondo Peak, situated at the western margin of the Rio Grande rift (Cole et al., 2005; Wolff and Gardner, 1995). The elevation of the La Jara catchment ranges from 2702 to 3429 m above sea level and encompasses an area of 367 ha draining the eastern portion of Redondo Peak.

The JRB-CZO has been used extensively to investigate connections among hydrologic partitioning, weathering and soil formation, the evolution of shallow and deep CZ architecture, and surface water dynamics (Chorover et al., 2011). Previous research in both the La Jara catchment and ZOB has shown that surface water chemistry and stable water isotopes emerging at the base of the La Jara catchment closely align with deeper groundwater chemical signatures measured in monitoring wells in the ZOB, indicating that deep groundwater routed through headwater catchments is the primary source of surface water baseflow in the greater La Jara catchment (Olshansky et al., 2018; White et al., 2019). The ZOB is bisected by a north-south trending normal fault, where the eastern half (represented by BH1) is comprised of fractured Bandelier Tuff (T) underlying a transition zone of weathered tuff (TZ), which is overlain by hydrothermally altered Bandelier Tuff (AT). Shallow hydrothermal alteration of Bandelier Tuff occurred shortly after the primary caldera-forming eruption [ca. 1.25 to 1.22 Ma; (Izett and Obradovich, 1994; Phillips et al., 2007; Spell et al., 1996)], during a period when an aerially extensive intra-caldera lake saturated shallow rocks with alkaline fluids, resulting in pervasive smectite-clinoptilolite-mordenite-silica type replacement across the VCNP extending only a few 10s of m from the surface (Chipera et al., 2008). In the western portion of Redondo Peak and the Valle Grande, deep-seated hydrothermal alteration consisted of propylitic- and phyllic-types of alteration, with high-level argillic hydrothermal alteration primarily consisting of illite, smectite, mixed-layer illite-smectite, kaolin, chlorite, quartz, pyrite, and hematite replacing weakly welded and porous units of the Bandelier Tuff (Hulen and Nielson, 1986; Hulen and Nielson, 1988). The western half of the ZOB (represented by BH2) is older, comprised of vesicular Bandelier Tuff (VT) overlain by ash (A) and volcanic breccias (VB, Fig. 1) (Bailey et al., 1969; Goff et al., 2011; Moravec et al., 2020; Smith and

Bailey, 1966). A soil/saprolite (S) layer across the ZOB extends to ca. 2 m depth at BH2 and ca. 5 m depth at BH1. The AT across the ZOB consists of smectite-clinoptilolite-mordenite-silica type replacement that extends to approximately 13 m at BH1 (Fig. 1) (Chipera et al., 2008; Moravec et al., 2020) and below 14 m (VT and A, under the VB) at BH2. The VB consists of interbedded sandstone lithics within pyroclastic surge deposits, exhibiting redoximorphic mottling, high calcite content (up to 17% by mass), and a complex depositional history (Hulen and Nielson, 1991; Moravec et al., 2020).

The ZOB elevation ranges from 2985 to 3097 m above sea level and was extensively burned during the 2013 Thompson Ridge wildfire that impacted significant portions of the VCNP and surrounding area (Cadol et al., 2015). The high-elevation, sub-humid climate of the site consists of a bimodal precipitation regime where approximately half of annual precipitation falls during the late North American summer monsoon and half falls as predominantly snow with some rain during the winter (Vazquez-Ortega et al., 2015; Zapata-Rios et al., 2015). Mean annual precipitation is 711 mm, and the mean average summer and winter temperatures are 10.7 and −1.1 °C, respectively (Zapata-Rios et al., 2015).

2.2. *Coring and subsampling of the weathering profile*

In June 2016, continuous cores were extracted from three locations within the ZOB (Fig. 1, BH1 and BH2 shown) to an approximate depth of 45 m using an LS 1000 tracked core rig with lined triple barrel coring and a TT diamond impregnated coring bit at an HQ3 diameter (core diameter: 61 mm; borehole diameter: 96 mm) (Moravec et al., 2020). Driller's depths, as measured from the drill platform, were corrected to a ground surface datum. In the field, continuous cores were subsampled by cutting 0.3 kg pucks with a water-cooled tile saw at intervals of approximately 40 to 80 cm. To eschew post sampling redox alteration, the pucks were stored in vacuum sealed aluminized mylar bags at 4 °C during transport to, and storage at, the University of Arizona. Subsamples for the batch weathering experiments were selected to encompass the variety of morphologies and mineralogies observed that comprise the active weathering profile at the two sites, which extends to approximately 15 to 18 m depth (Moravec et al., 2020). In addition to these samples, deep subsamples from approximately 35 m from BH1 and 2 were included in the laboratory experiments to quantify insipient weathering reactions within the relatively unweathered, fractured portions of the profile.

2.3. *Batch experiments*

Subsamples for laboratory experiments were taken from stored drill core pucks by scooping approximately 50 g of material from the mylar bags using a clean scupula (wiped with 100% ethanol and Kimwipe™). Samples were dried at 53 °C in a drying oven overnight before being "lightly crushed" in a ceramic mortar and pestle to separate clods, and stored in re-sealable Ziploc® bags at room temperature (25 °C). Batch weathering experiments were conducted in duplicate, with some samples run in triplicate (20 samples). Samples were weighed and placed in 50 mL acid-washed, metal-free conical centrifuge tubes (VWR®). Ultrapure water (18.2 MΩ, Nanopure™, Barnstead™) was pre-equilibrated with atmospheric air for 5 d under constant bubbling, prior to being added to the tubes to give suspensions with a solid to solution mass ratio of 1:20 (e.g., 2.5 g solids and 50 g solution) and a headspace volume of approximately 5 cm^3. Ultrapure water equilibrated with atmospheric CO_2 and O_2 was selected as the aqueous reactant to simulate interactions with water that was initially aggressive (i.e., highly undersaturated with respect to mineral constituents), and representative of meteoric precipitation and snowmelt. This approach provides a consistent time zero baseline for comparison across diverse samples from the weathering profile. In addition to carbonic acid, low molecular weight organic acids are also known to affect the rates and trajectories of biogeochemical mineral weathering reactions (Drever, 1994; Drever and Stillings, 1997). We chose not to include any organic acids in our pore water simulant because these constituents vary greatly in their concentrations in time and space, and they significantly decrease in relative importance with depth from the surface soil to groundwater at our site (Olshansky et al., 2018).

Contact of the solid material with aqueous reactant defined the start time for each experiment. Tubes containing the water/mineral suspension were rotated gently in an end-over-end rotating mixer at 7 RPM (to minimize inter-particle abrasion) for the full duration of each of six-time intervals: 1, 4, 24, 336, 1344, and 8760 h. Samples reacted for more than 24 h were uncapped daily and allowed to equilibrate with atmospheric air for approximately 1 h to replenish headspace and dissolved CO_2 and O_2. The 8 week and 1 y samples were uncapped daily and equilibrated with air for the first four weeks of reaction time, and then left unopened for the duration of the experiments to reduce the likelihood of sample loss. Removal of solids by centrifugation marked the ending time for each batch reaction. Suspensions were transferred to 1.5 M HNO_3 acid-washed 50 mL polypropylene (PP), round bottom centrifuge tubes (Nalgene ® model no. 3110-9500) and centrifuged for 10 min at 49,000 relative centrifugal force (RCF). The supernatant solution was then transferred using disposable pipettes from the centrifuge tubes to clean, acid-washed 50 mL PP centrifuge tubes, and centrifuged again for 10 min at 49,000 RCF. The supernatant solution was transferred again to acid washed, metal free 50 mL centrifuge tubes. Particle sizes retained in the supernatant were estimated to be less than 270 nm based on Stokes' law settling velocities assuming spherical particles with an average density of 2.65 g cm^{-3} (Whittig and Allardice, 1986). Sample solutions recovered from 4 h and 1 y reactions were centrifuged twice following the procedure above. The supernatant solutions were then serially filtered first through 450 nm GHP membrane Acrodisc polyethersulfone syringe filters (Pall Corporation, Westborough, MA, USA), with an aliquot of filtrate collected, using disposable transfer pipettes, in acid washed 15 mL centrifuge vials, for chemical analysis to capture colloid chemistry (operationally defined here as between 25 and 450 nm). The 450 nm filtrate was then vacuum filtered through 25 nm mixed cellulose ester membrane filters (VSWP 047 00, Millipore Corporation, MA, USA) to capture dissolved chemistry. Supernatant solutions and filtrates were acidified using 0.15 M HNO_3 (Ari-Star Plus, VWR®) and analyzed for total element concentrations at the University of Arizona Laboratory for Emerging Contaminants (ALEC) by inductively coupled plasma mass spectrometer (ICP-MS, Agilent 7700×, Santa Clara, CA). Total element analysis included: Li, Be, B, Na, Mg, Al, Si, P, K, Ca, Ti, V, Cr, Mn, Fe, Co, Ni, Cu, Zn, Ga, Ge, As, Se, Rb, Sr, Zr, Nb, Mo, Ag, Cd, In, Sn, Sb, Cs, Ba, Hf, Tl, Pb, Bi, Y, La, Ce, Pr, Nd, Sm, Eu, Gd, Tb, Dy, Ho, Er, Tm, Yb, Lu, and ^{238}U by ICP-MS; F^-, Cl^-, NO_2^-, Br^-, NO_3^-, PO_4^{3-}, and SO_4^{2-} by ion chromatography (Dionex ICS-6000, Sunnyvale, CA). Total organic carbon (TOC), total inorganic carbon (TIC), and total nitrogen (TN) were also measured for supernatant and filtrate solutions using a Shimadzu TOC-L Carbon/Nitrogen Analyzer (Shimadzu USA Manufacturing, Inc., Canby, Oregon), however, these data were affected by organic carbon leaching from filter materials and, therefore, are not included here. While colloids are strictly defined as entities ranging from 1 to 1000 nm in effective diameter, we limit our operational definition herein to particles ranging in size from 25 to 450 nm, due to sample volume limitations and the common use of 450 and 25 nm filtration by practitioners in the field.

Analytical QA/QC protocols for all ICP-MS analyses were adapted from US EPA Method 200.8. Calibration standards were prepared from multi-element stock solutions (SPEX Certiprep, Metuchen, NJ). Calibration curves include at least seven data points with correlation coefficients >0.995. The QC protocol included a continuing calibration blank (CCB), a continuing calibration verification (CCV) solution and at least one quality control sample (QCS) to be analyzed just after calibration, again after every 12 samples, and at the completion of the run. The QCS solutions are from an independent source, such as NIST SRM

1643e - Trace elements in water, or QCS solutions from High Purity Standards (Charleston, SC). Acceptable QC responses must be between 90 and 110% of the certified value. Lastly, a suitable internal standard (usually Rh, In, Ga or Ge) is added using on-line addition into the sample line and mixing tee.

2.4. BET specific surface area

Chemical release from reacted solid samples into solution for each timestep was normalized to the Brunauer–Emmett–Teller (BET) specific surface area (SSA) of the unreacted sample. To measure SSA, samples were degassed under N_2 at 105 °C for at least 2 h using a Micromeritics FlowPrep 060 prior to measuring specific surface area (SSA) by the N_2 BET adsorption method with a liquid N_2 bath (Gemini VII 2930p, Micromeritics Instrument Corp., Norcross, GA, USA). Instrument SSA precision and accuracy was confirmed after every five samples using a known SSA standard (black carbon, SSA = 21.75 $m^2\ g^{-1}$) with comparison to reported values.

2.5. Calculation of reaction rates

Rate coefficients were determined on the basis of reaction rates measured for chemical releases, in accordance with Eq. (1) (Sparks, 2003):

$$R_{diss} = SA \bullet k_e (1-\Omega) \tag{1}$$

where R_{diss} is the rate of mineral dissolution [μmol s^{-1}], *SA* is the surface area of solids [m^2] (measured prior to reaction and held constant for each reaction timestep), k_e is the rate coefficient for element *e* in μmol $m^{-2}\ s^{-1}$, and Ω is the relative saturation of solution with respect to a given mineral. The relative saturation is given by

$$\Omega = \frac{Q}{K} \tag{2}$$

where *Q* is the reaction quotient and *K* is the reaction equilibrium constant for a given mineral dissolution reaction at 25 °C (laboratory room temperature). Initial (far from equilibrium) reaction rates were determined using the aqueous concentrations for the first two data points in the time series (i.e., $t = 0$ and 4 h), where $Q \ll K$ for primary minerals (e.g., plagioclase, K-feldspar, and calcite), saturation indices (SI) were $\ll 0$, and $\Omega \rightarrow 0$, such that Eq. (1) becomes:

$$R_{diss} = SA \bullet k_e \tag{3}$$

and

$$k_e = \frac{R_{diss}}{SA} \tag{4}$$

Rate coefficients were assumed to be zero order.

2.6. Mineralogical changes during batch reaction

Reacted and residual solids from samples reacted for 1 y were freeze dried and milled below 50 μm using a vibrating ZrO_2 ceramic ball mill for 20 min. Colloids from 1 y samples were collected after serial filtration (Section 2.3) by rinsing 25 nm filters with ultrapure water into acid-washed 50 mL centrifuge vials, where after they were freeze dried and milled. Milled samples were mounted onto transparent tape as random oriented mounts following Moravec et al. (2020) and analyzed by synchrotron transmission X-ray diffraction (XRD) at the Stanford Synchrotron Radiation Lightsource (SSRL) beamline 11–3 using a corundum internal standard (except colloids) at a mass ratio of 1:5 corundum: sample. X-rays were generated by a 2-Tesla wiggler, using side-scattering Si(311) monochromator at fixed energy of 0.976 Å (12.7 keV). Samples were exposed to a 100 $μm^2$ beam for 30 s under constant raster motion in front of a 345 mm diameter CCD image plate detector with 73.24 $μm^2$ pixel and calibrated using a lanthanum hexaboride (LaB_6) standard. Laue patterns (2D) were converted to 2-theta diffractograms (1D) using the Nika v1.81 add-on (Ilavsky, 2012) with Igor Pro v 8.02 (WaveMetrics, Inc. Portland OR), energy converted to Cu-Kα radiation for conventional comparisons, and minerals quantified (Q-XRD) using the Reitveld refinement module in X'Pert HighScore Plus (Malvern Panalytical) as described in Hayes et al. (2014). Normalized (crn_{113}) weathered Q-XRD data were compared to normalized bulk, unreacted Q-XRD diffractograms to estimate changes in mineral content over the 1 y reaction time by differential X-ray diffraction (D-XRD) (Schulze, 1981). To account for instrument drift and differences in peak counts, XRD data were aligned based on corundum internal standard peak positions, then normalized based on the quantitative corundum internal standard content. Estimates of changes in mineral content (Eq. (5)) were calculated based on peak area differences (Figs. S1–S22):

$$\Delta min = \frac{M_{hkl,t1} - M_{hkl,t0}}{M_{hkl,t0}} \tag{5}$$

where *Δmin* is the change in mineral content for mineral *M*, $M_{hkl,t1}$ is the peak area at 1 y and $M_{hkl,t0}$ is the peak area for unreacted samples.

2.7. Electron microprobe analysis and mineral stoichiometry calculations

Electron microprobe analysis (EMPA) of select core samples was performed at the University of Arizona Lunar and Planetary Laboratory - Electron Microprobe Laboratory using a CAMECA SX100 Ultra electron probe microanalyzer. Microprobe images were collected at a 15 kV accelerating voltage, 20 nA sample current, and a beam size of 2 μm. Elemental abundance was determined by wavelength dispersive spectroscopy (WDS) at the specific energy levels for each element, calibrated to internal standards (Domanik et al., 2004). Thin sections were cut from samples cast in metal free epoxy (Epotek 301-2FL), glued to quartz slides, and milled to thickness of 30 μm by Spectrum Petrographics, Inc. (Vancouver, WA). For EMPA analysis, slides were coated with 7 nm of carbon. Mineral stoichiometries were calculated from microprobe elemental abundances using the standard methods in Deer (2013).

2.8. Solid sample geochemistry

Solid samples were analyzed for total geochemistry as reported in Moravec et al. (2020). Samples were dry crushed in the University Arizona Geochronology Lab using a steel mortar and pestle, sieved below 250 μm, and further milled to less than 50 μm using a ZrO_2 ball mill for 20 min. Analytical triplicates were fused with lithium metaborate ($LiBO_2$) at a mass ratio of 1:20 (e.g., 0.05 g sample and 1.0 g $LiBO_2$) in a Katanax® K1 Prime $LiBO_2$ furnace, heated to 1000 °C for 2 min, and the molten pellet was transferred to 1.5 M HNO_3 to fully dissolve the sample. Dissolved samples were then diluted on an analytical balance using 0.15 M HNO_3 solutions prepared with ultrapure water (18.2 MΩ, Nanopure™, Barnstead™). Samples were analyzed (including QA/QC protocols, as stated in Section 2.3) by ICP-MS as above.

2.9. Stoichiometry of cation release

The extent of (non-)stoichiometric cation release into aqueous solutions for weathering reactions was calculated on the basis of normalization to Na in solution and in the unreacted solid phase following Pohlmann et al. (2016):

$$\xi_{aq/s} = log\left(\frac{[X]_{aq}/[Na]_{aq}}{[X]_{s}/[Na]_{s}}\right) \tag{6}$$

where $\xi_{aq/s}$ provides a measure of stoichiometric cation release to solution, $[X]_{aq}$ and $[Na]_{aq}$ are aqueous phase concentrations, and $[X]_s$ and $[Na]_s$ are solid phase concentrations.

2.10. Serial Filtration

The fractional contribution of colloids (defined here operationally as 25–450 nm in equivalent diameter) to element release was determined from the difference in concentration of elements in 450 nm and 25 nm filtrates:

$$C_r = \left(1 - \frac{C_{<25nm}}{C_{<450nm}}\right) \tag{7}$$

where C_r is the colloidal fraction, and $C_{<25nm}$ and $C_{<450nm}$ are the element concentrations (μmol m^{-2}) measured in the corresponding filtrate solutions.

2.11. Geochemical modeling

Geochemical modeling of aqueous solutions was performed using PHREEQC geochemical modeling software (Parkhurst and Appelo, 1999). Saturation indices (SI) were calculated at sample pH and reaction temperature (25 °C) using the MINTEQ geochemical database of thermodynamic constants (with the exception for zeolite minerals, which used the LLNL database provided in PHREEQC, which did not change the results) assuming aqueous solutions comprised truly dissolved species, and are reported as

$$SI = log\Omega \tag{8}$$

where SI is the saturation index and Ω is the relative saturation (Eq. (2)). The geochemical databases of thermodynamic constants in PHREEQC use end-member stoichiometries for smectites and zeolites calculations, therefore the SI values for these minerals may be viewed as approximations for the non-ideal stoichiometric smectite and zeolite minerals collected at the JRB-CZO.

3. Results

3.1. Mineral content

Electron microprobe images of the core sample from BH1 (Fig. 2, panels A and B, 1A-5Q-2, 4.16 mbgs, AT), show the mineral assemblage contains primarily Ca/K clinoptilolite, K-mordenite, and montmorillonite within the matrix, which surrounds larger feldspar grains, primarily anorthoclase, sanidine, and albite. K-feldspar is intergrown within plagioclase grains, which has been replaced by K-bearing zeolites at grain surfaces (Fig. 2, panel B). Replacement of feldspars with zeolites was commonly observed within hydrothermally altered mineral assemblages located within the upper 15 m of BH1 (i.e., AT, Fig. 1) in the eastern portion of the ZOB (Moravec et al., 2020). Zeolites in BH1 also contain quantifiable amounts of Ba, Fe, Mg, Ti, and Mn (Table 1), suggesting these constituents were either incorporated into the zeolite structure during their formation, or were sequestered during subsequent ion exchange reactions. Smectite was also identified coating feldspar grains. The EMPA measured stoichiometries that were less than 100% had significant hydroxide or water present in the structure.

Electron microprobe images of core samples from BH2 show that the upper 14 m (VB, Fig. 2, panel C, 2A-8Q-8, 8.18 mbgs) consisted primarily of quartz grains surrounded by a mixture of small feldspars (K-feldspar), mica (primarily annite and phlogopite), Fe (oxyhydr)oxides, and clustered calcite nodules. Quartz grains were rounded to subrounded consistent with physical and chemical weathering prior to

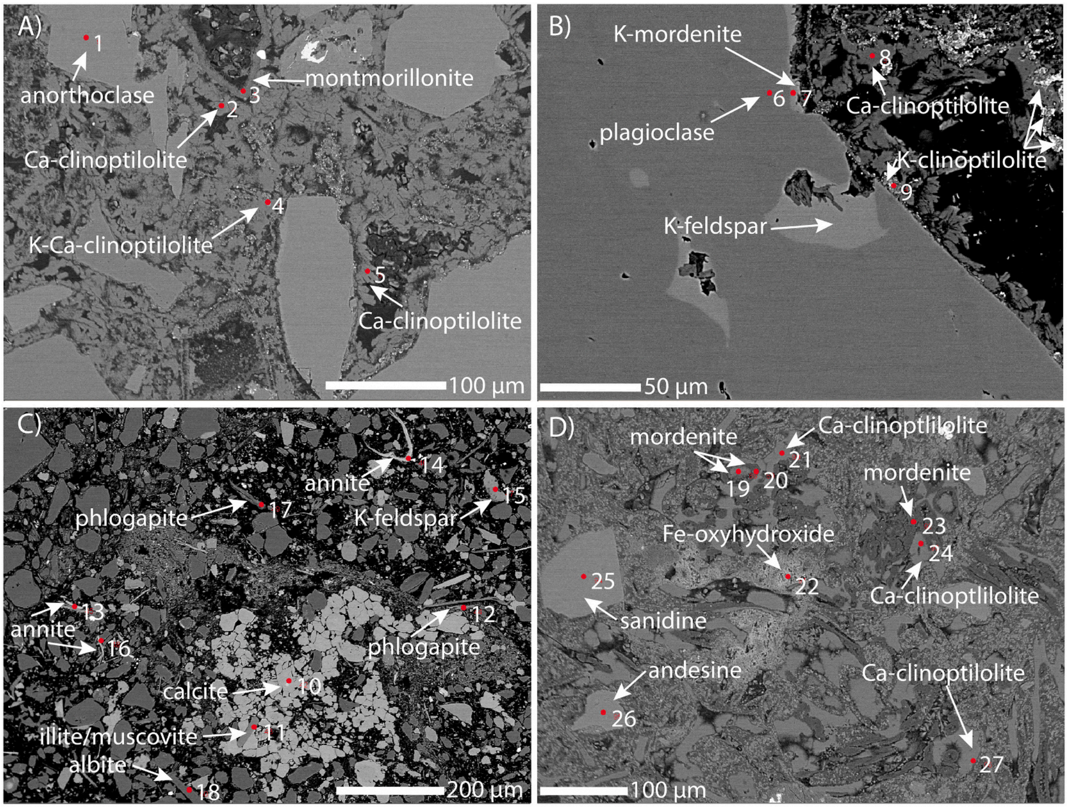

Fig. 2. Microprobe images and identified minerals for BH1 and BH2. Panels (A) and (B) are images of sample 1A-5Q-2 (4.16 mbgs; AT), which contains a variety of zeolites and feldspars consistent with hydrothermally altered mineral assemblages located within the upper 15 m of BH1. Panel (C) is an image of sample 2A-8Q-8 (8.18 mbgs) located within the VB that comprised the upper 14 m of BH2. Panel (D) is an image of sample 2A-27Q-4 (35.21 mbgs), which is located within VT of BH2. Mineral chemical formulae shown in panels A – D are provided in Table 1.

Table 1
Chemical formulae for mineral samples (Fig. 2) by EMPA.

Sample (Depth, m)	Number (Fig. 2)	Mineral	Chemical formula	Recovery (%)
1A-5Q-2 (4.16 mbgs; AT)	1	Anorthoclase	$K_{0.27}Na_{0.67}Ca_{0.01}Fe_{0.01}Al_{1.07}Si_{2.93}O_8$	101.01
	2	Ca-clinoptilolite	$Na_{0.02}K_{0.75}Ca_{1.74}Ba_{0.02}Fe_{0.06}Mg_{0.52}Mn_{0.01}[Al_{6.26}Si_{29.92}O_{72}](Cl_{0.06})\cdot xH_2O$	83.60
	3	Montmorillonite	$K_{0.16}Ca_{0.07}Na_{0.01}(Al_{1.78}Mg_{0.17}Fe_{0.63}Si_{3.53}O_{10})([OH]_{1.96}Cl_{0.04})\cdot xH_2O$	75.41
	4	Ca-K-clinoptilolite	$Na_{0.36}K_{1.39}Ca_{1.56}Ba_{0.02}Fe_{0.03}Mg_{0.02}[Al_{5.44}Si_{30.66}O_{72}]\cdot xH_2O$	84.49
	5	Ca-clinoptilolite	$Na_{0.03}K_{1.11}Ca_{1.64}Ba_{0.02}Fe_{0.05}Mg_{0.54}Mn_{0.02}[Al_{5.81}Si_{30.19}O_{72}](Cl_{0.01})\cdot xH_2O$	84.89
	6	Plagioclase	No data	–
	7	K-mordenite	$K_{9.89}Ca_{0.01}Na_{0.05}Fe_{0.02}[Al_{10.15}Si_{37.87}O_{96}]\cdot xH_2O$	101.97
	8	Ca-clinoptilolite	$Ca_{2.27}K_{0.59}Na_{0.16}Mg_{0.012}Fe_{0.03}Ba_{0.03}[Al_{6.58}Si_{29.71}O_{72}](Cl_{0.05})\cdot xH_2O$	59.25
	9	K-clinoptilolite (Fe^{3+} Exchanged)	$K_{2.73}Ca_{0.70}Na_{0.60}Ba_{0.04}Ti_{0.23}Mg_{0.51}Mn_{0.05}[Al_{7.54}Fe_{5.99}Si_{24.15}O_{72}](Cl_{0.16})\cdot xH_2O$	83.06
2A-8Q-8 (8.18 mbgs; VB)	10	Calcite	$Ca_{0.97}Mn_{0.03}CO_3$	53.46
	11	Illite/Muscovite	$Na_{0.6}K_{0.86}Ca_{0.02}(Al_{2.65}Mg_{0.11}Fe_{0.10}Ti_{0.05}Si_{3.10}O_{10})(OH)_2$	95.29
	12	Phlogopite	$Na_{0.02}K_{0.14}Ca_{0.07}(Al_{1.51}Mg_{1.78}Fe_{0.87}Ti_{0.15}Mn_{0.02}Si_{2.58}O_{10})([OH]_{1.99}Cl_{0.01})$	85.43
	13	Annite	$Na_{0.03}K_{0.36}Ca_{0.05}(Al_{1.57}Mg_{1.34}Fe_{1.10}Ti_{0.10}Mn_{0.02}Si_{2.59}O_{10})([OH]_{1.99}Cl_{0.01})$	87.97
	14	Annite	$Na_{0.01}K_{0.47}Ca_{0.05}(Al_{1.59}Mg_{0.95}Fe_{0.93}Ti_{0.12}Mn_{0.03}Si_{2.85}O_{10})([OH]_{1.95}Cl_{0.05})$	77.29
	15	K-feldspar	$K_{0.56}Na_{0.39}Al_{1.05}Si_{2.97}O_8$	97.45
	16	Annite	$Na_{0.01}K_{0.70}Ca_{0.03}(Al_{1.50}Mg_{0.81}Fe_{1.30}Ti_{0.08}Mn_{0.03}Si_{2.69}O_{10})([OH]_{1.99}Cl_{0.01})$	94.80
	17	Phlogopite	$Na_{0.01}K_{0.03}Ca_{0.07}(Al_{1.61}Mg_{2.04}Fe_{0.69}Ti_{0.04}Mn_{0.01}Si_{2.66}O_{10})(OH)_2$	85.37
	18	Albite	$Na_{0.99}Al_{1.03}Si_{2.97}O_8$	98.18
2A-27Q-4 (35.21 mbgs; VT)	19	Mordenite	$K_{0.34}Ca_{1.43}Na_{1.19}Fe_{0.45}Mg_{0.33}Ti_{0.03}Mn_{0.03}[Al_{6.87}Si_{41.19}O_{96}]\cdot xH_2O$	79.33
	20	Mordenite	$K_{0.44}Ca_{0.31}Na_{0.06}Fe_{2.13}Mg_{0.98}Ti_{0.07}Mn_{0.03}[Al_{5.68}Si_{41.28}O_{96}]\cdot xH_2O$	65.40
	21	Ca-clinoptilolite	$Na_{0.14}K_{0.13}Ca_{1.63}Mg_{0.06}[Al_{5.78}Si_{30.75}O_{72}]\cdot xH_2O$	86.58
	22	Fe-oxyhydroxide (*non-stoich.*)	$Fe_{0.68}(Ca_{0.01}Mg_{0.02}K_{0.06}Al_{0.11}Si_{0.37})OOH$	67.78
	23	Mordenite	$K_{0.31}Ca_{0.25}Na_{0.14}Fe_{1.57}Mg_{0.73}Ti_{0.05}Mn_{0.02}[Al_{4.35}Si_{42.89}O_{96}]\cdot xH_2O$	68.96
	24	Ca-clinoptilolite	$Na_{0.57}K_{0.19}Ca_{1.59}Mg_{0.06}Mn_{0.02}[Al_{5.82}Si_{30.60}O_{72}]\cdot xH_2O$	90.39
	25	Sanidine	$K_{0.52}Na_{0.46}Ca_{0.01}Al_{1.02}Si_{2.98}O_8$	100.72
	26	Andesine	$K_{0.06}Na_{0.55}Ca_{0.37}Al_{1.37}Si_{2.62}O_8$	100.16
	27	Ca-clinoptilolite	$Na_{0.13}K_{0.06}Ca_{1.56}Mg_{0.08}[Al_{5.81}Si_{30.76}O_{72}]\cdot xH_2O$	91.99

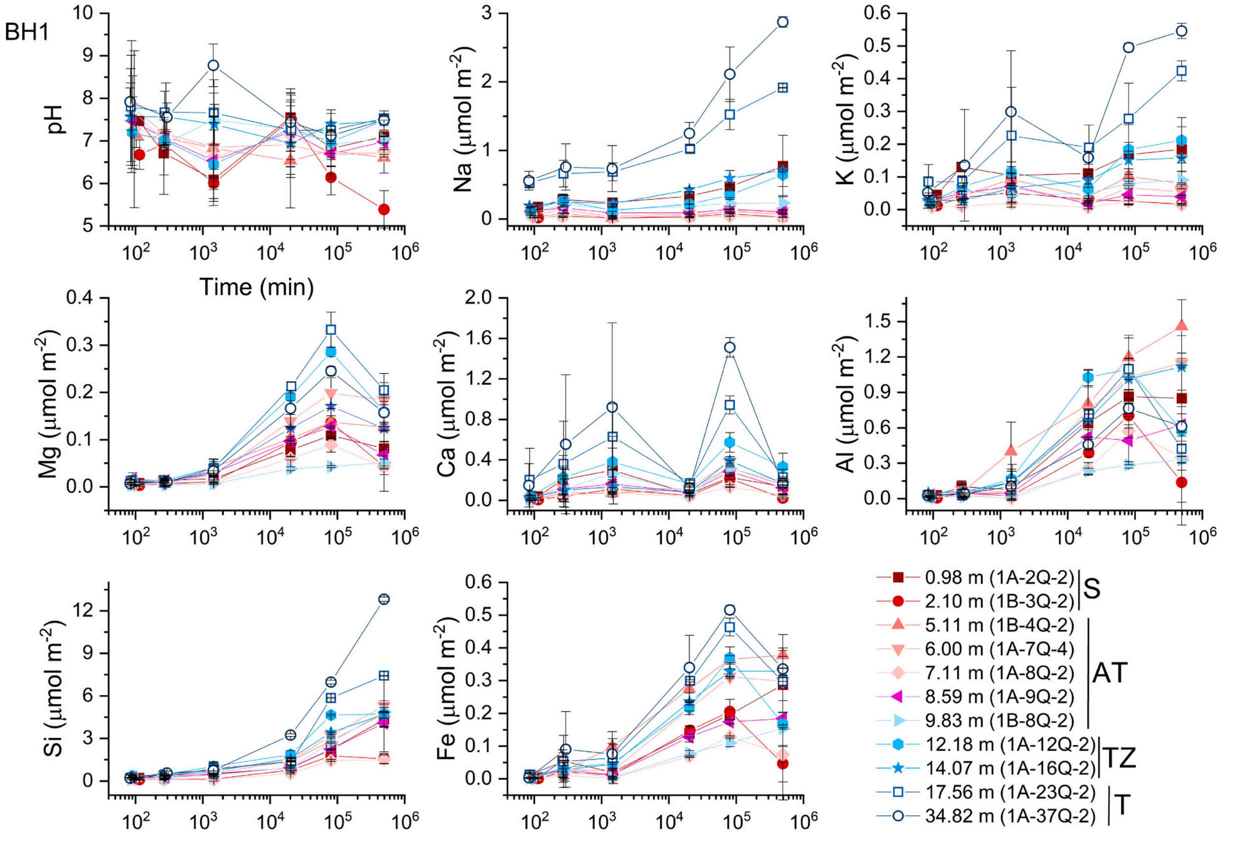

Fig. 3. Elemental release to porewater (μmol m^{-2}) during 1 y weathering experiment for extracted core samples from BH1 (Eq. (4)). Symbols and error bars represent mean and standard deviation (n = 2 or 3). Closed symbols represent matrix dominated CZ (<15 m) and open symbols represent fracture dominated CZ (>15 m). Lithologic groups align with Fig. 1 mineral composition for BH1. Samples were centrifuged at 49,000 RCF for 10 min 2 times (particle size <270 nm based on Stokes' law, see Section 2.3 for details).

deposition. Micas exhibited frayed edges; however, clay minerals were not uniquely identifiable by microprobe analysis. Below 14 m, the VT (panel D, Fig. 2, 2A-27Q-4, 35.21 mbgs) consisted of feldspar grains (sanidine and andesine) with Ca-clinoptilolite and mordenite within the matrix and Fe (oxyhydr)oxides coating fracture surfaces. Smectite was not identified in this sample by EMPA, however, 1.4 nm d-spacing (hkl_{001}) 2:1-layer type phyllosilicates (e.g., smectite) were identified by XRD in significant amounts in the deeper profile (BH2, Fig. 1).

3.2. Batch reaction chemical release

Ultrapure water was equilibrated with atmospheric air for 5 d prior to experimental weathering, and initial pH was 5.6 for all samples. Patterns observed in geochemical dissolution time series of major ions were generally consistent across depths within a given borehole, with lower elemental release in the upper, more weathered portions of the profiles (i.e., S, AT, TZ, VB, and A) and higher release in the deeper, less weathered portions of the profiles (i.e., T and VT). Chemical release of major ions (shown as aqueous concentrations normalized by SSA) at all depths initially increased with reaction time coincident with proton production (decreasing pH) (Figs. 3 and 4, respectively). Solutions from the longest reaction times (1 y) showed lower concentrations for Mg, Ca, Al, and Fe for BH1 samples, and Mg, Al, and Fe for BH2 samples compared to the previous data point (e.g., 8 wk) results. Values of pH for BH 1 samples generally ranged from 7 to 8 initially, decreasing with time to 6.5 to 7.5 (Fig. 3), whereas BH2 pH values were relatively alkaline initially (8 to 9.5) for samples in the upper 14 m (i.e., VB), and then decreased to ca. 8 over time (Fig. 4). Samples in the upper 14 m of BH2 had relatively low chemical release (Si, Al, K, Na, and Fe) over the experimental time period, with the exception of Mg and Ca, which likely represents calcite and magnesium calcite dissolution in VB portion of BH2. Less chemical release was observed for the upper 15 m of BH1 than for deeper samples from either BH1 or BH2, however, the general patterns of chemical release were similar across the profile at BH1 (Fig. 3). Ca release in BH1 increased until 2 weeks into the experiment, where after it decreased significantly, and increased again in long term reactions (8 wks and 1 yr). The deepest samples for both boreholes had significantly higher chemical release relative to samples in the upper portions of the profiles.

Initial element release rates (from 0 to 4 h, Eq. (4)) varied by borehole, element, and depth (Fig. 5 and 6, panels B–H). In general, BH1 had higher release rates for Si, Al, and Mg compared to BH2. Rates were higher at lower depths (T and VT) compared to the more weathered or altered shallow depths (e.g. <15 m; S, AT, TZ, VB, and A).

3.3. Batch reaction mineral changes

Differential X-ray diffraction (D-XRD) data showed that (with some exceptions) 1 y of batch reaction resulted in diminution of feldspars and zeolites, whereas 1.4 nm 2:1-layer type phyllosilicates, calcite, and amorphous SiO_2 either showed net decrease or increase depending on the sample depth (Figs. 5 and 6, panel J). Amorphous SiO_2 was quantified using the cristobalite peak, crs_{101}, due to the occurrence of pedogenic/hydrothermal amorphous SiO_2 and cristobalite commonly associated with secondary montmorillonite and zeolites derived from high silica volcanic ash (Henderson, 1971). BH1 had the largest mineral transformation from ca. 5 to 12 m depth corresponding to high Al release (Fig. 5, panel D), whereas BH2 saw the largest mineral transformation in the upper 5 m of the profile corresponding to high Al and Si release (e.g., 1.73 mbgs) (Fig. 6, panels D and E). Mineral masses

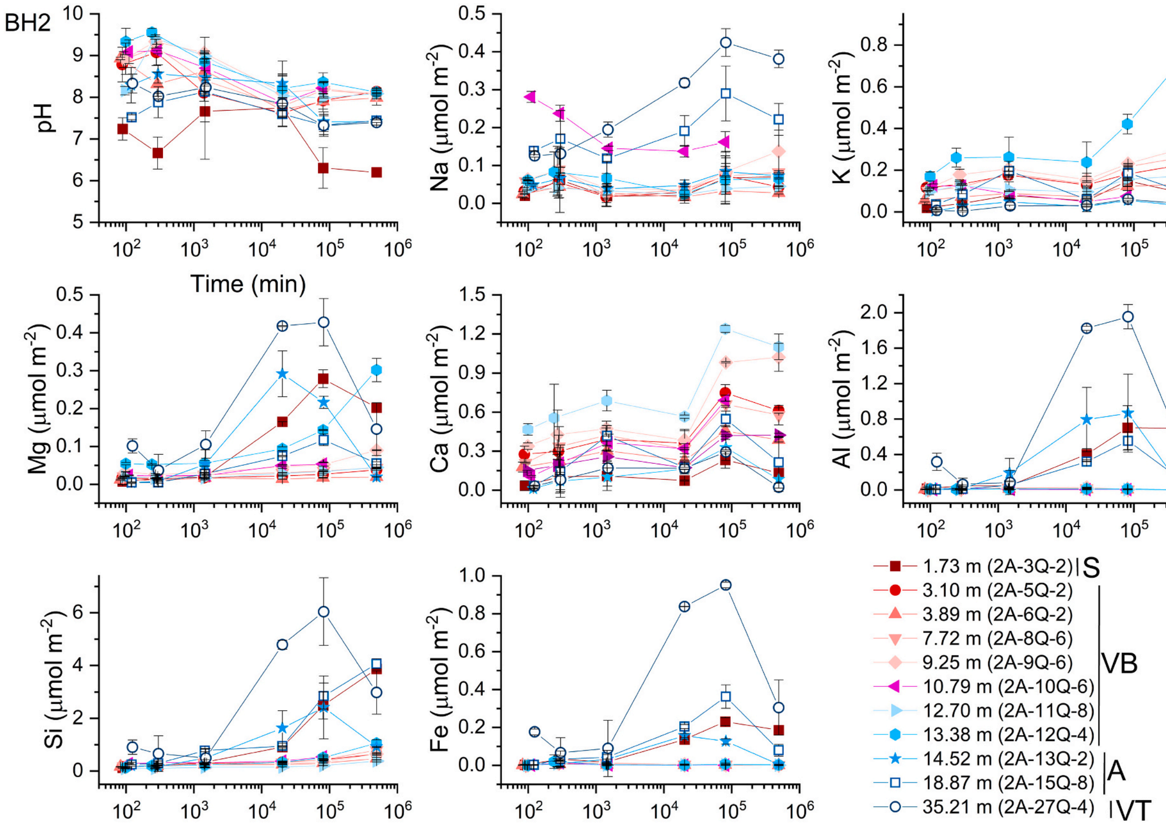

Fig. 4. Elemental release to porewater (μmol m^{-2}) during 1 y weathering experiment for extracted core samples from BH2 (Eq. (4)). Symbols and error bars represent average and standard deviation (n = 2 or 3). Closed symbols represent matrix dominated CZ (<15 m) and open symbols represent fracture dominated CZ (>15 m). Lithologic groups align with Fig. 1 mineral composition for BH2. Samples were centrifuged at 49,000 RCF for 10 min 2 times (particle size <270 nm based on Stokes' law, see Section 2.3 for details).

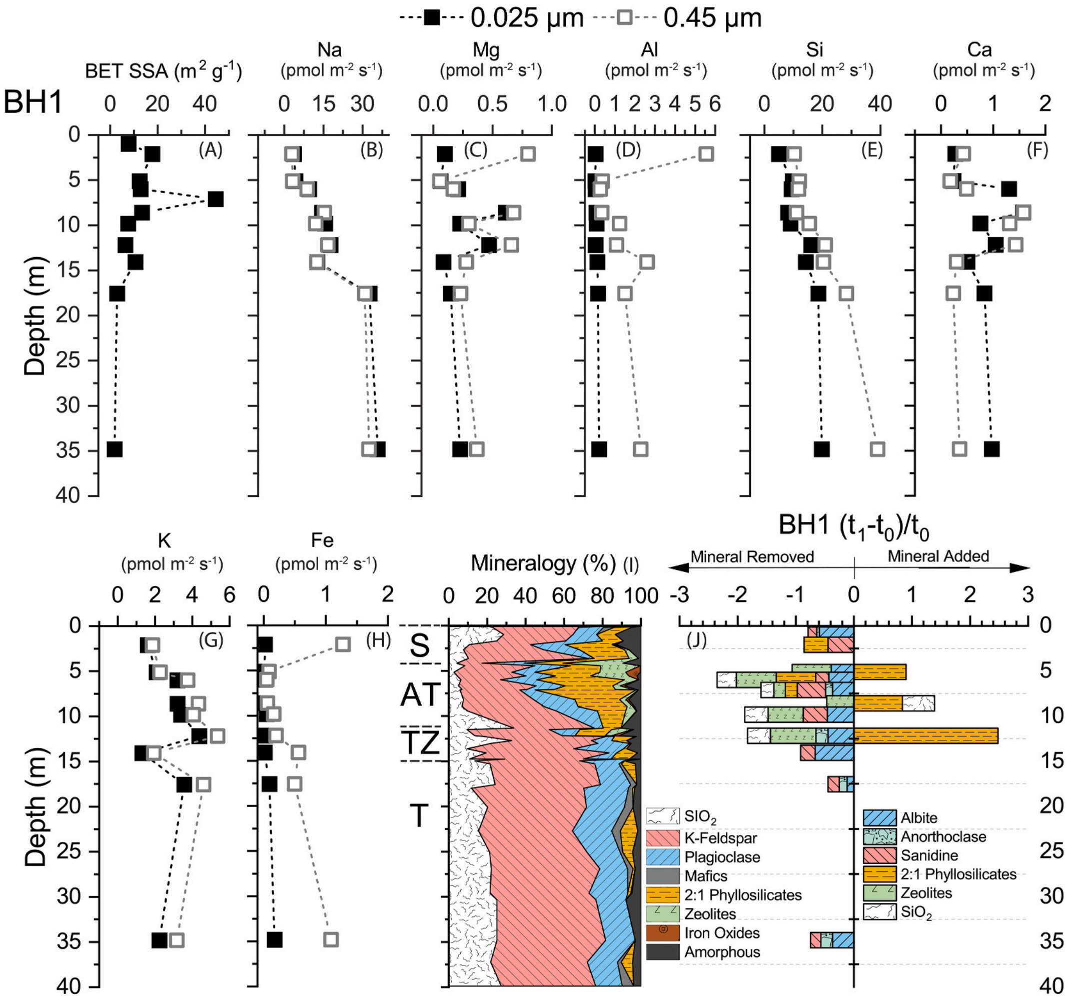

Fig. 5. Borehole 1 BET specific surface areas (Panel (A); Table SI-1), zero-order rate coefficients for Na, Mg, Al, Si, Ca K, and Fe normalized to BET surface areas (Panels B-H; Eq. (4); Table SI-2), and D-XRD (J) determined changes in mineral composition of bulk samples after 1 y of reaction (Eq. (5), Figs. S1–22) as a function of depth. Minerals weathered/removed [$(t_1 - t_0)/t_0$] during reaction are shown as negative values and minerals added are positive values. Bulk mineralogy with depth (I) is included for reference with stratigraphic zones, identified based on geochemistry and mineralogy of bulk core samples shown where lithologic groups align with Fig. 1 mineral composition for BH1 (adapted from Moravec et al., 2020). 2:1 phyllosilicates included indiscriminate 1.4 nm d-spacing (hkl_{001}) clay minerals (Moravec et al., 2020) later identified as smectite. Upper 15 m are matrix dominated (i.e., weathered material with matrix dominated hydrologic flow) and 15 m to depth is fracture dominated.

removed from BH1 were primarily feldspars (albite, anorthoclase, and sanidine), zeolites, and amorphous SiO_2. Mineral accumulation in BH1 was observed to occur primarily for 2:1 layer-type phyllosilicates (and SiO_2 for 8 m sample) from ca. 5 to 10 m depth.

Mineral transformations in BH2 were dominantly associated with calcite and 1.4 nm 2:1-layer type phyllosilicates in the upper 14 m, with calcite precipitated at 10 m (Fig. 6, panel J). Calcite precipitation at 10 m is consistent with supersaturation of filtrate solutions with respect to calcite (data not shown). The upper 14 m contained calcite in the bulk solids (up to 17% by mass) and calcite nodules were observed to be present in microprobe images taken of samples within this depth interval (Fig. 2, panel C). Below 14 m, where calcite was no longer present, mineral dissolution consisted primarily of feldspar and zeolites (e.g. albite, anorthoclase, sanidine, and mordenite). 1.4 nm 2:1 layer-type phyllosilicates precipitated at 15 m depth, which coincided with albite and sanidine dissolution at the same depth.

3.4. Colloidal contributions to element release

Filterable colloids (25 nm < "colloid" < 450 nm) represented significant fractions of total elemental concentrations (Eq. (6)) with magnitude depending on the element. Colloids represented up to 99% of total Al and Fe released to aqueous solution during the batch experiments for BH1 and BH2 (Fig. 7). BH1 had the highest colloidal Al and Fe for the 1 y reacted samples. A significant portion of colloidal Al and Fe was dispersed shortly after the weathering reactions began (as shown on Fig. 7 at 4 h) suggesting that these colloids were present in unreacted samples and were dispersed in the initial stages of the experiment. However, a significant increase in colloidal Fe, Al, Mg, Ca, K, and Mn with reaction time from 4 h to 1 y also suggests colloidal neoformation. Consistent with prior work on stream systems, e.g., Trostle et al. (2016), Na was not retained in the colloidal fraction in BH1 or BH2 and was consistently dissolved (<25 nm).

In the upper 15 m of BH2 (within the VB), significant fractions of released Al, Fe, and Si (>75%, >50%, and ca. 20 to 25%, respectively) were in colloidal form during the initial stages of weathering (i.e. 4 h), but this fraction of the total then decreased substantially by 1 y (Fig. 7). Concentrations of Al, Fe, and Si in this section of the profile were low compared to VT samples (Fig. 4), and that of Al and Si appeared to be completely dissolved (rather than colloidal) after 1 y (Fig. 7).

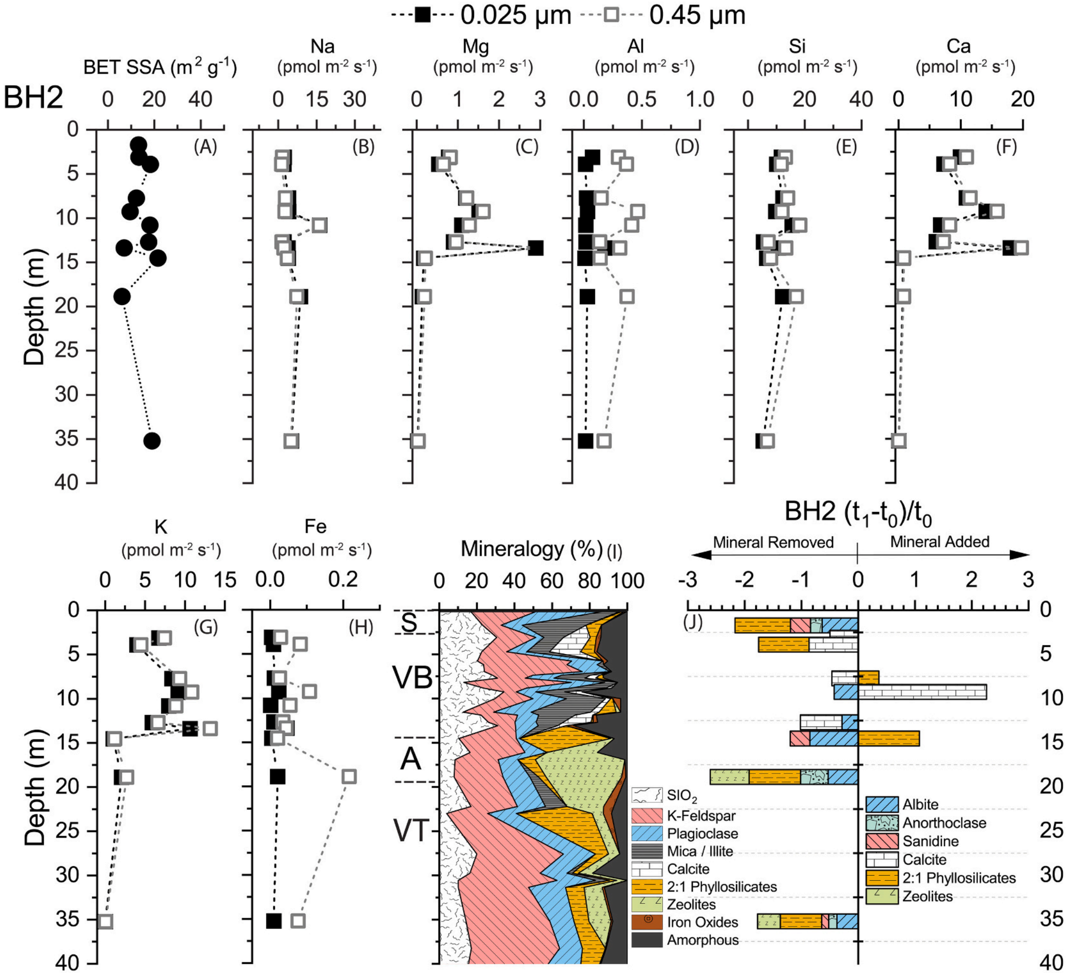

Fig. 6. Borehole 2 BET specific surface areas (Panel (A); Table SI-1), zero-order rate coefficients for Na, Mg, Al, Si, Ca K, and Fe normalized to BET surface areas (Panels B-H; Eq. (4); Table SI-2), and D-XRD (J) determined changes in mineral composition of bulk samples after 1 y of reaction (Eq. (5), Figs. SI-1–22) as a function of depth. Minerals weathered/removed $[(t_1 - t_0)/t_0]$ during reaction are shown as negative values and minerals added are positive values. Bulk mineralogy with depth (I) is included for reference with stratigraphic zones, identified based on geochemistry and mineralogy of bulk core samples shown where lithologic groups align with Fig. 1 mineral composition for BH2 (adapted from Moravec et al., 2020). 2:1 phyllosilicates included unclassified 1.4 nm d-spacing (hkl_{001}) clay minerals (Moravec et al., 2020) later identified as smectite. Upper 19 m are matrix dominated (i.e., weathered material with matrix dominated hydrologic flow) and 19 m to depth is fracture dominated.

4. Discussion

4.1. Colloidal release

Throughout the volcaniclastic weathering profiles in the study catchment, metasomatic minerals (e.g., zeolites, smectites, amorphous SiO_2, etc.) with high specific surface areas played a key role in aqueous geochemical response to freshwater infusion. These minerals were present initially as coatings on primary mineral surfaces (Fig. 2, panels A and B) but upon introduction of dilute water, they were dispersed into suspension and subject to dissolution. This resulted in supersaturation of the aqueous phase and neoformation of colloidal precipitates stable under the conditions of the experiment. Colloidal dispersion and precipitation of neoformed colloids were detected in core samples from AT, T, VT, and VB after 1 y of experimental weathering. Molar Si:Al ratios of the colloidal fractions $[(Si/Al)_{colloid}]$ in AT (<14 m, BH1 and >15 m, BH2) ranged from 5 to 10 during early reaction times (4 h), which is characteristic of zeolites (e.g., clinoptilolite and mordenite) (Fig. 8). Incongruent dissolution of these zeolites formed colloidal smectites (Si:Al $\sim$ 2), after 1 y of experimental weathering, which incorporated K, Ca, Mg, Mn, and possibly Fe into their sheets and interlayers (Figs. 5, 6 and 7). Precipitation of smectite was quantifiable by D-XRD at three depths in the AT at BH1 (Fig. 5); however, smectite precipitation was not detectable in the T due to small XRD peaks in both weathered and unweathered samples. Excess Si from the zeolite to smectite transformation remained in the dissolved fraction. Dispersion of colloidal Fe (oxyhydr) oxides occurred in short term (e.g., 4 h) experiments in the AT and T; the Fe content in the dissolved (<25 nm) fraction was much lower than the colloidal (25–450 nm) fraction (Fig. 7). After 1 y of experimental weathering, Fe (oxyhydr)oxides precipitated as neoformed colloids (25–450 nm) had removed nearly all Fe from the dissolved fraction (i.e. <25 nm), as reflected in a decrease in the $(Si/Fe)_{colloid}$ ratio from 4 h to 1 y (Fig. 8).

Similarly, in BH2 VB (Fig. 6) (<14 m depth), colloidal dispersion occurred at early reaction time (4 h), likely as a mixture of SiO_2, feldspars, and clay (illite and smectite). In contrast to AT and T, after 1 y of experimental weathering, the colloidal fraction, in some cases, revealed a 10-fold *increase* in Si:Al ratios (Fig. 8). This is attributed to the predicted precipitation and aggregation of gibbsite, which is in contrast to BH1 where zeolite dispersion and subsequent weathering led to smectite precipitation. Whereas 25 nm filtrates were undersaturated $(SI < 0)$ with respect to gibbsite at 4 h, equilibrium $(SI = 0)$ was observed for the 25 nm filtrates at 1 y (Fig. 9), consistent with the reduction in dissolved Al concentrations. Molar Al concentrations decreased with time for VB

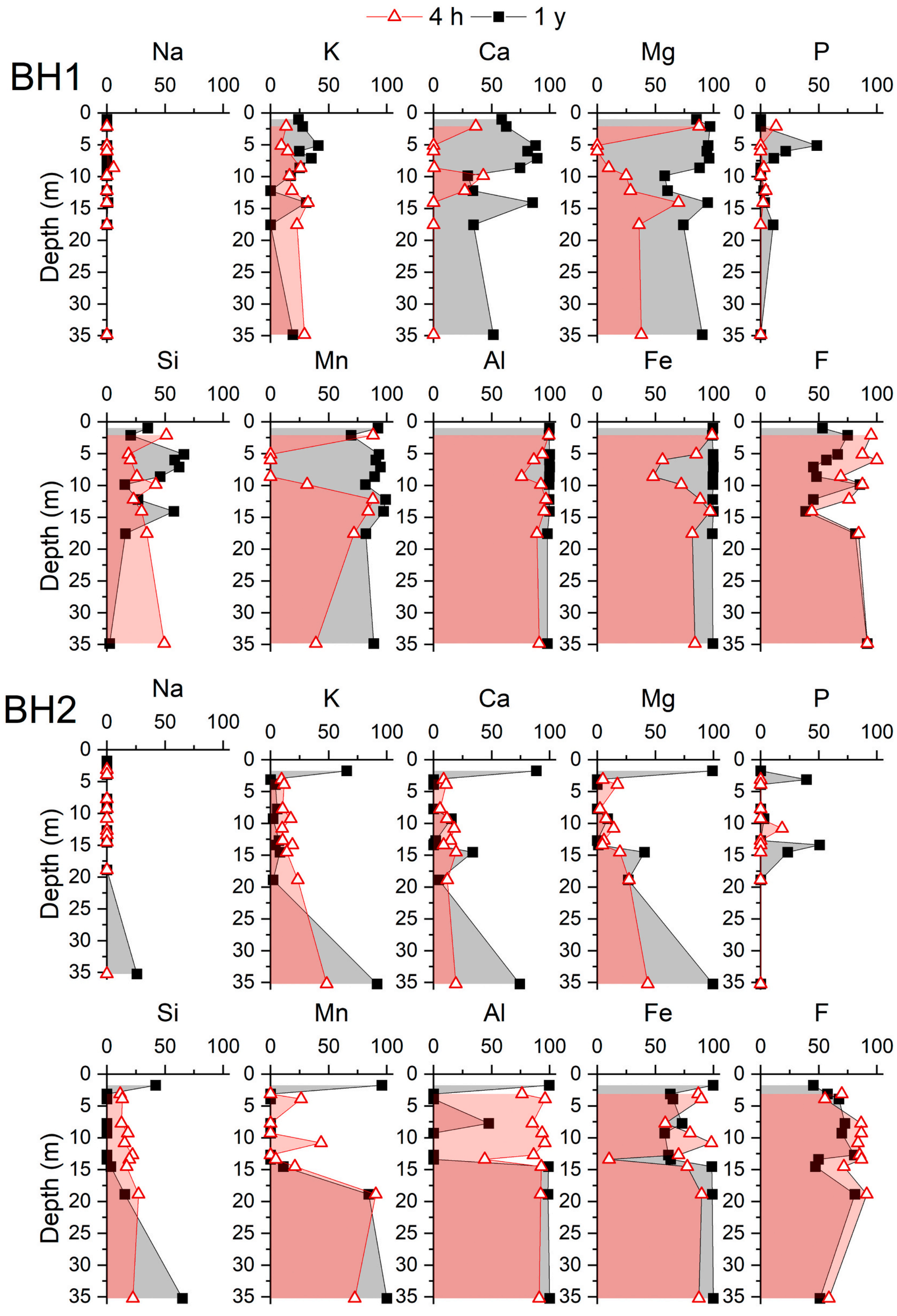

Fig. 7. Colloidal fraction (25–450 nm) of major elements released to solution during batch reactions. Open triangles (red shaded areas) are for samples reacted for 4 h; closed squares (grey shaded areas) are samples reacted for 1 y. Scales on x-axes are percentage of element contained in the colloidal fraction, shaded to show colloidal fraction. (For interpretation of the references to color in this figure legend, the reader is referred to the web version of this article.)

experimental weathering (Fig. 4; 3 to 14 m depth), and precipitated gibbsite colloids likely aggregated such that they were captured during 450 nm filtration (filtering took much longer, up to several hours, for these samples compared to samples without gibbsite precipitates), which would explain the near total removal of Al from both colloidal and dissolved fractions (Goldberg, 1989). Although some Fe (oxyhydr) oxides appear to have precipitated in T suspensions after 1 y, colloidal Fe (oxyhydr)oxides appear to have been dispersed during the early stages of experimental weathering and remained so over the full year of experimental weathering. While colloids are expected to contribute to

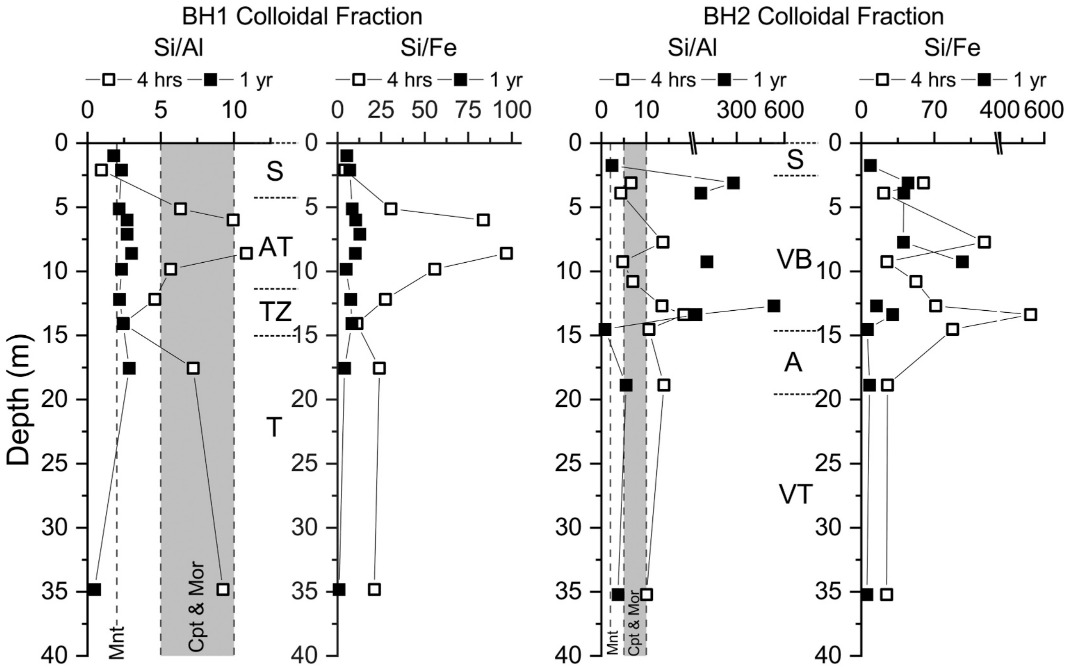

Fig. 8. Molar ratios of Si/Al and Si/Fe of the colloidal fraction (from 450 to 25 nm) at BH1 and BH2. Molar ratios for montmorillonite (2, Mnt) and clinoptilolite/mordenite (ranging from 5 to 10, Cpt & Mor) are shown for reference. Stratigraphic zone designations are included to denote changes in mineralogy and geochemistry. Note broken x-axes for BH2 Si/Al and Si/Fe.

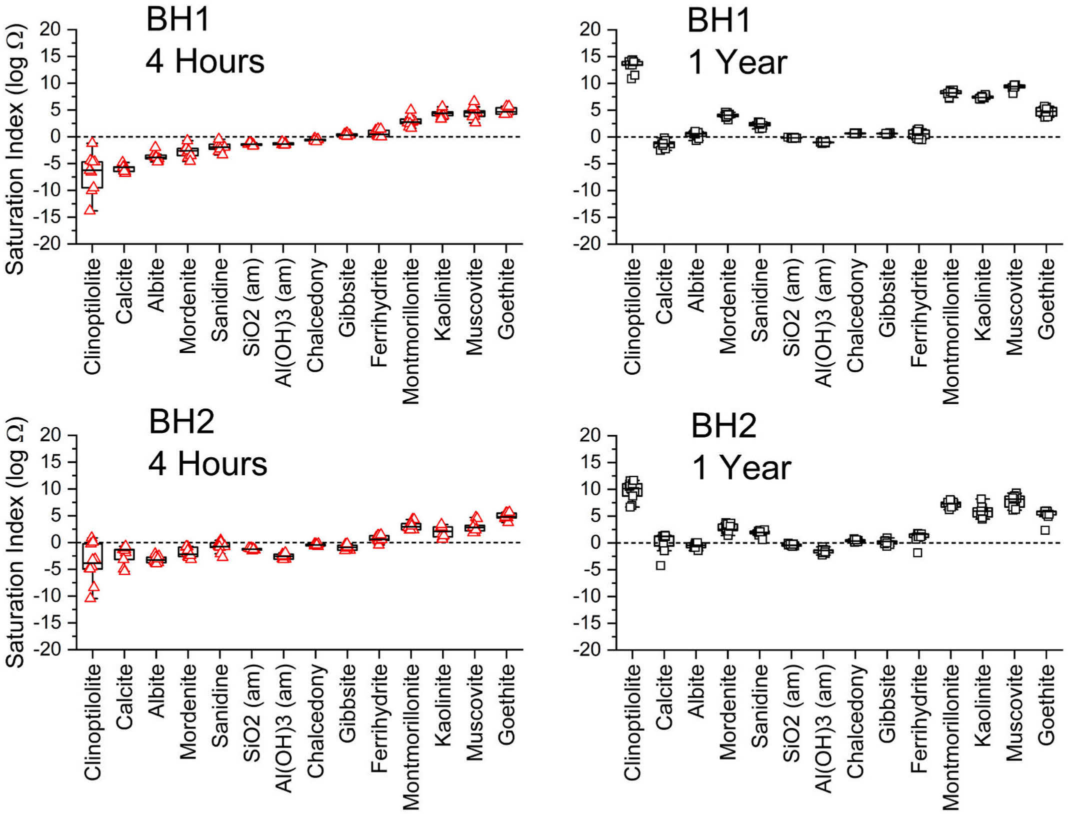

Fig. 9. Modeled mineral saturation indices (logΩ) of pore waters from BH1 and BH2 after 4-h and 1-y weathering reactions based on geochemical modeling of solutions subjected to 25 nm filtration (defined here operationally as the "truly dissolved" fraction). Modeled mineral saturation indices for 450 nm filtrates are presented in SI for comparison (Fig. SI–23). SI > 0 indicates supersaturated solutions and thermodynamic tendency for precipitation; SI < 0 indicates undersaturation and tendency for dissolution. Box and whiskers show statistical variability of modeled SI (e.g. mean, 25th and 75th quartiles [box], and 5th and 95th quartiles [whiskers]), n = 22.

450 nm filtrate concentrations for hydrolyzing cations (Al, Fe, Mn), it is noteworthy that even non-hydrolyzing cations (particularly Ca, Mg, but also K) showed non-negligible fractions in the colloidal pool. Of interest is the fact that the colloidal fraction of Ca and Mg increased with time throughout BH1 and also at depth in BH2 (Fig. 7), consistent with the formation of phyllosilicate clays with significant capacity for cation exchange. Such a response is also predicted from geochemical modeling, as discussed below.

The colloidal contribution to what is commonly interpreted as an apparent dissolved ion activity highlights the previously recognized fact that a 450 nm cutoff, commonly used to separate particles and solutes under standard methods does not accurately represent the truly dissolved fraction of aqueous solutions (Guo and Santschi, 2007; Trostle et al., 2016). Therefore, use of 450 nm filtrates tends to yield higher SI values than are calculated using 25 nm filtrates (Fig. SI–23). Hence, hereafter, we have restricted our geochemical modeling to the concentrations measured in the 25 nm filtrates as a means to assess changes in mineral stability.

Short-term reactions initially gave rise to solutions that were undersaturated ($SI < 0$) with respect to most primary minerals present in the cores (e.g., calcite, feldspars, and amorphous SiO_2). However, over 1 y of weathering time these solutions reached saturation ($SI = 0$) or supersaturation ($SI > 0$) for many of the same phases, and exhibited growing supersaturation with time for secondary metal oxyhydroxides and phyllosilicates (Fig. 9). Even as early as 4 h, solutions were supersaturated with respect to goethite and secondary phyllosilicates (kaolinite and montmorillonite), and the supersaturation values increased with time, consistent with D-XRD evidence of smectite precipitation for several samples (Figs. 5 and 6). The data are consistent with feldspar weathering to form kaolinite, and dissolution of zeolites to form smectite (e.g., montmorillonite). By way of comparison, modeled mineral SIs for 450 nm filtrates (Fig. SI–23) were generally higher than for the 25 nm filtrates, with solutions now showing (super)saturated conditions ($SI \geq 0$) with respect to many minerals for which solutions were found to be undersaturated when using the 25 nm filtrates (e.g., clinoptilolite, albite, mordenite, sanidine, amorphous $Al(OH)_3$, chalcedony, and gibbsite). This highlights the importance of defining a dissolved fraction that is consistent with the intrinsic assumptions inherent in thermodynamic geochemical speciation models.

4.2. Weathering rates and reactions

Elemental release rates and patterns were dependent on primary and secondary mineral composition, which varied as a function of depth and geology (Figs. 2, 5 and 6). Zeolites, albite, anorthoclase, sanidine, and 1.4 nm phyllosilicates were the minerals most susceptible to dissolution across the boreholes; however, with varying elemental release rates as a function of sample location. BH1 elemental release rates were greater than BH2 due to the abundance of hydrothermal secondary minerals in BH1, which have faster weathering rates (Graham et al., 1988). These faster release rates corresponded to higher aqueous concentrations and the precipitation of neoformed smectite in AT and T. High Ca release rates for the VB in BH2 corresponded with nearly complete removal of calcite from reacted samples (Fig. 6). Calcite dissolution and precipitation has been proposed to control hydrochemical response to seasonal climate forcing in the upper 15 m of the profile at BH2, supported by high Ca and HCO_3^- concentrations in shallow groundwater at this site (Olshansky et al., 2018; White et al., 2019).

In both BH1 and BH2 (Figs. 5 and 6), higher elemental release rates at depths greater than 15 m resulted from unweathered, fresh mineral surfaces deeper in the profile being exposed to aggressive waters (i.e., CO_2-charged, low ionic strength and undersaturated with respect to the mineral assemblage of the tuff) during experimental weathering. Smaller elemental release rates in upper sections of the profiles is likely due to secondary mineral coatings that protect the underlying primary minerals against weathering (Fig. 2) (Dorn, 2013; Weaver, 1978) and lower prevalence of weatherable materials. The largest release rates were observed for the deepest samples, which contained the least weathered materials and least protective coatings, with the highest proportion of primary silicates compared to secondary minerals (Moravec et al., 2020), and likely represent incipient dissolution of the T.

Elemental release rates measured for volcaniclastic materials from the ZOB varied across the major elements (Figs. 5 and 6; summarized in Table SI–2), and rate differences provide insight into incongruent dissolution reactions. Average release rates for Si after 4 h of experimental weathering for BH1 and BH2 (filtered <25 nm) were −10.95 and −11.03 log mol m^{-2} s^{-1}, respectively, and release rates for K were −11.59 and −11.53 log mol m^{-2} s^{-1}, respectively (Table SI–2). Comparing these rates to BET SSA normalized experimental weathering rates using crushed samples, as recorded in the literature, they are consistent with observed plagioclase (−11.54 log mol m^{-2} s^{-1}, ±0.39, n = 7) and K-feldspar (−12.07 log mol m^{-2} s^{-1}, ±0.87, n = 3) weathering reaction rates from several locations comprised from fresh granitic rock to weathered saprolite (White et al., 2001). The highest Si release rate (observed for the deepest samples [ca. 35 m] from BH1), was −10.70 log mol m^{-2} s^{-1}, which was slightly higher than the fastest albite and K feldspar weathering rates reported by White et al. (2001) [between −11 and − 12 log (mol m^{-2} s^{-1})]. Incongruent dissolution reactions for K-feldspar weathering to kaolinite (Eq. (9)) and plagioclase weathering to montmorillonite [Eq. (10), shown with calculated stoichiometry from sample 1A-5Q-2 (4.16 m, Table 1)] illustrate that Si release rates should be roughly double the K release rates for K-feldspar weathering to kaolinite and near unity for Na with albite weathering to montmorillonite.

$$4KAlSi_3O_8 + 4H^+ + 18H_2O \rightarrow Si_4Al_4O_{10}(OH)_{8(s)} + 8Si(OH)_4^0 + 4K^+ \tag{9}$$

$$\begin{aligned} &NaAlSi_3O_8 + 0.78Al(OH)_2^+ + 0.16K^+ + 0.07Ca^{2+} + 0.17Mg^{2+} + 0.63Fe^{3+} \\ &\quad + 0.53Si(OH)_4^0 \\ &\quad + 0.32H_2O \rightarrow K_{0.16}Ca_{0.07}Na_{0.01}\left(Al_{1.78}Mg_{0.17}Fe_{0.63}^{(III)}Si_{3.53}O_{10}\right)(OH)_{2(s)} \\ &\quad + 0.99Na^+ + 2.32H^+ \end{aligned} \tag{10}$$

Na and Si release rates were near unity for BH1 and the deeper, VT samples from BH2 (Table SI–2). Release rates of K were generally about 5 times lower, with the exception of samples from 3 to 13 m in BH2 (within the VB), which were close to unity. This suggests that incongruent reactions illustrated in Eqs. (9) and (10) are consistent with data deriving from the initial phases of the experiment. We also postulate that precipitation of secondary minerals coupled with SiO_2, zeolite, and/or glass weathering may be occurring.

D-XRD analysis indicated that plagioclase, K-feldspar, zeolite, and amorphous SiO_2 were all subjected to varying degrees of dissolution, which explains the slightly larger Si release compared to Na and K with smectite precipitation. Electron microprobe images of the VT showed feldspars present as both larger clasts and in the fine-grained matrix (Fig. 2, panel D), mixed with volcanic glass. Fine-grained textures have higher surface area compared to larger clasts and may promote faster dissolution kinetics. Coupled with volcanic glass dissolution, the fine-grained, feldspar-rich matrix may account for mineral dissolution and high elemental release rates for samples from the deeper CZ.

Analysis of the stoichiometry of element release to aqueous solution relative to bulk solid chemistry provides some insight into potential mechanisms for observed differences in elemental release rates at various reaction time steps and the chemical composition of filtrates. The short- and long-term experiments showed that some elements readily release to solution (P and K), but most major cations (Mg, Ca, Si, Fe, Mn, and Al) are largely retained in the solid phase (Fig. 10). It is not surprising that stoichiometric, congruent dissolution of the average bulk mineral composition for each sample, where $\xi_{aq/s} = 0$ (Eq. (6)), did not occur (Fig. 10, upper panels). This is consistent with mineral

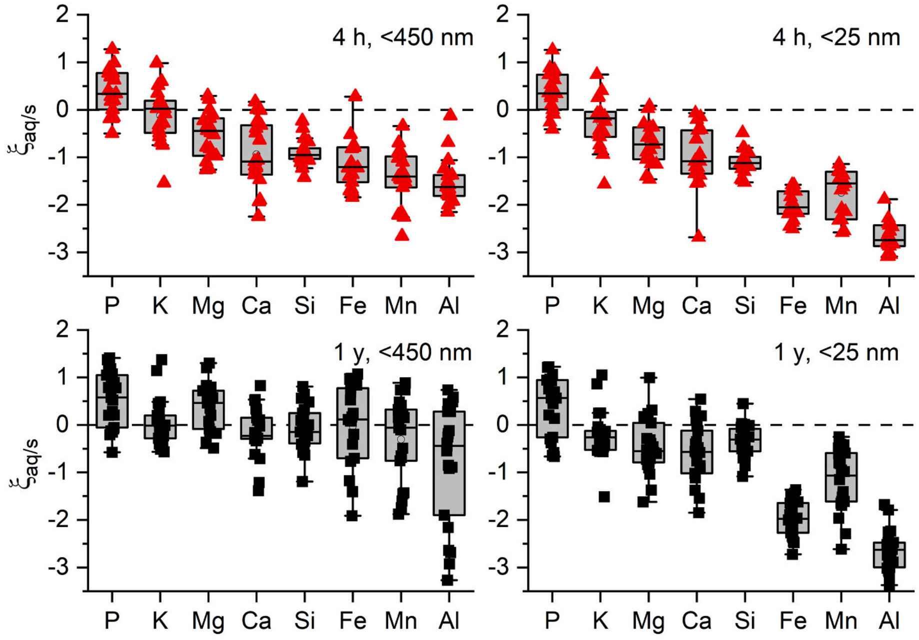

Fig. 10. Stoichiometry of elemental release to aqueous solutions (combined BH1 and BH2) during experimental weathering relative to solid phase geochemistry, normalized to Na ($\xi_{aq/s}$, Eq. (6)). Negative values represent net element retention in the solid phase and positive values represent net element release, in both cases relative to Na, which is considered to remain in solution upon release and not re-precipitated. Stoichiometric elemental release is represented by the horizontal dashed line at 0. Upper panels are <450 nm (left) and <25 nm (right) filtrates after 4 h of weathering; the lower panels are <450 nm (left) and <25 nm (right) filtrates after 1 y of weathering. Box and whisker plots show mean (central line in box), median (open circles), 25th and 75th quartiles (boxes), and outliers (whiskers).

transformations discussed above. It is noteworthy, however, that the <25 nm filtrates exhibited a larger non-stoichiometric release (i.e., more negative $\xi_{aq/s}$) compared to <450 nm filtrates wherein Fe, Mn, and Al were mostly contained in the colloidal fraction (25 to 450 nm) (Fig. 10). Solid phase retention of Mg, Ca, Si, Fe, Mn, and Al for the short-term weathering experiments may also result from a combination of factors: 1) differential mineral weathering rates, 2) cation exchange on surfaces, and 3) incongruent mineral dissolution reactions, in addition to elemental retention in the colloidal fraction.

After 1 y of experimental weathering, the <450 nm filtrates appeared to approach aqueous stoichiometric equilibrium with respect to the bulk solids (i.e., $\xi_{aq/s} \sim 0$), with few samples retaining Ca, Fe, Mn, and Al in the solid phase (comprising of the deeper T and VT samples from both BH1 and BH2, where $\xi_{aq/s}$ is negative; Fig. 10, lower left panel). However, for <25 nm filtrates, element retention in the solid phase was significantly greater than for <450 nm filtrates (between 1 and 3 orders of magnitude) for Mg, Ca, Fe, Mn, and Al (Fig. 10), indicating that the difference is due to colloidal components. Importantly, this shows that the polyvalent cations Al, Fe, Mn, Si, and Mg dominate the colloid chemistry (including dispersed and neoformed colloids), with a mineral composition of smectite, sanidine, quartz, cristobalite, mordenite, and likely some poorly crystalline gibbsite (Fig. SI–24). Moreover, the Si/Al ratio of the colloid fraction (Fig. 8) ranged from 2.2 to 3.0, which is comparable to that for the montmorillonite as shown in Eq. (10) (Si/Al = 3.0; BH1 ~ 4.2 m), and much lower than the Si/Al ratio of suspended zeolites (Fig. 8). It is likely that isomorphic substitution of Mg, Fe, and Mn for Al in octahedral sheets occurred within the newly formed, colloidal smectite structure, providing structural surface charge and cation exchange sites for K and Ca. This provides a mechanism for the observed increase in cation retention within the colloidal fraction in BH1 from 4 h to 1 y (Fig. 7).

4.3. Solute chemistry evolution with time compared to stream, spring, and groundwater

Results of the batch weathering reactions show that solute chemistry changed over relatively short time frames (Fig. 11). Comparing surface and groundwater (ellipses in Fig. 11) base-cation proportions from the field [data from White et al., 2019] with batch weathered samples (data points in Fig. 11) corresponding to BH2 (<14 m) and shallow groundwater align within the first few hours of reaction, with insignificant changes over 1 y of reaction (Fig. 11). Ca-rich water coupled with calcite mineral dissolution in shallow BH2 samples (Fig. 5) indicate that shallow groundwater chemistry is controlled by calcite dissolution/precipitation reactions in the VB with relatively rapid reaction kinetics. The absence of shallow groundwater at BH1 limited direct comparison between field conditions and batch weathered samples; however, shallow BH1 (<14 m) batch reaction chemistry exhibited significant variation over the experimental period (Fig. 11). From the experimental results, BH1 shallow sample water chemistry was most similar to deep BH2 water chemistry, both of which derive from comparable, hydrothermally altered secondary mineral assemblages (e.g. smectite and zeolites). In contrast, batch reaction water chemistry for deep BH1 samples was relatively unrelated to any groundwater chemical signatures collected from the field. This suggests that batch weathering results for deep BH1 samples correspond to primary mineral weathering reactions as these samples were crushed with fresh mineral surfaces available to chemical attack by aggressive meteoric water. In the field, the deeper portions of BH1 are fracture dominated with Fe (oxyhydr) oxides and Mn oxides coating surfaces, preventing aggressive water from contacting primary minerals. In contrast, batch water chemistry for samples <14 m in BH1, was relatively close to deep groundwater chemistry in BH1 wells. This suggests that groundwater that passes through the AT develops its chemical signatures near the surface as a result of interaction with smectite and zeolites. Once this solute-rich water reaches the deep groundwater reservoir, it retains this shallow CZ signature due to reduced reaction rates (with high aqueous Si activity diminishing most silicate weathering) and rock shielding by Fe (oxyhydr)oxide and Mn oxide coated fractures, and so does not change considerably over time. In addition, colloids transported into the deep CZ likely form aggregates and mask reactive mineral surfaces, as observed in clay fracture coatings for some samples in extracted cores from BH1 (Moravec et al., 2020). Fractured rock aquifers may more generally exhibit similar hydrochemical behavior as oxyhydroxide and clay coatings on fracture surface have been found to be prevalent in many CZ environments (Buss et al., 2013; Dorn, 2013; Frazier and Graham, 2000; Hasenmueller et al., 2017; Kim et al., 2006; Weaver, 1978).

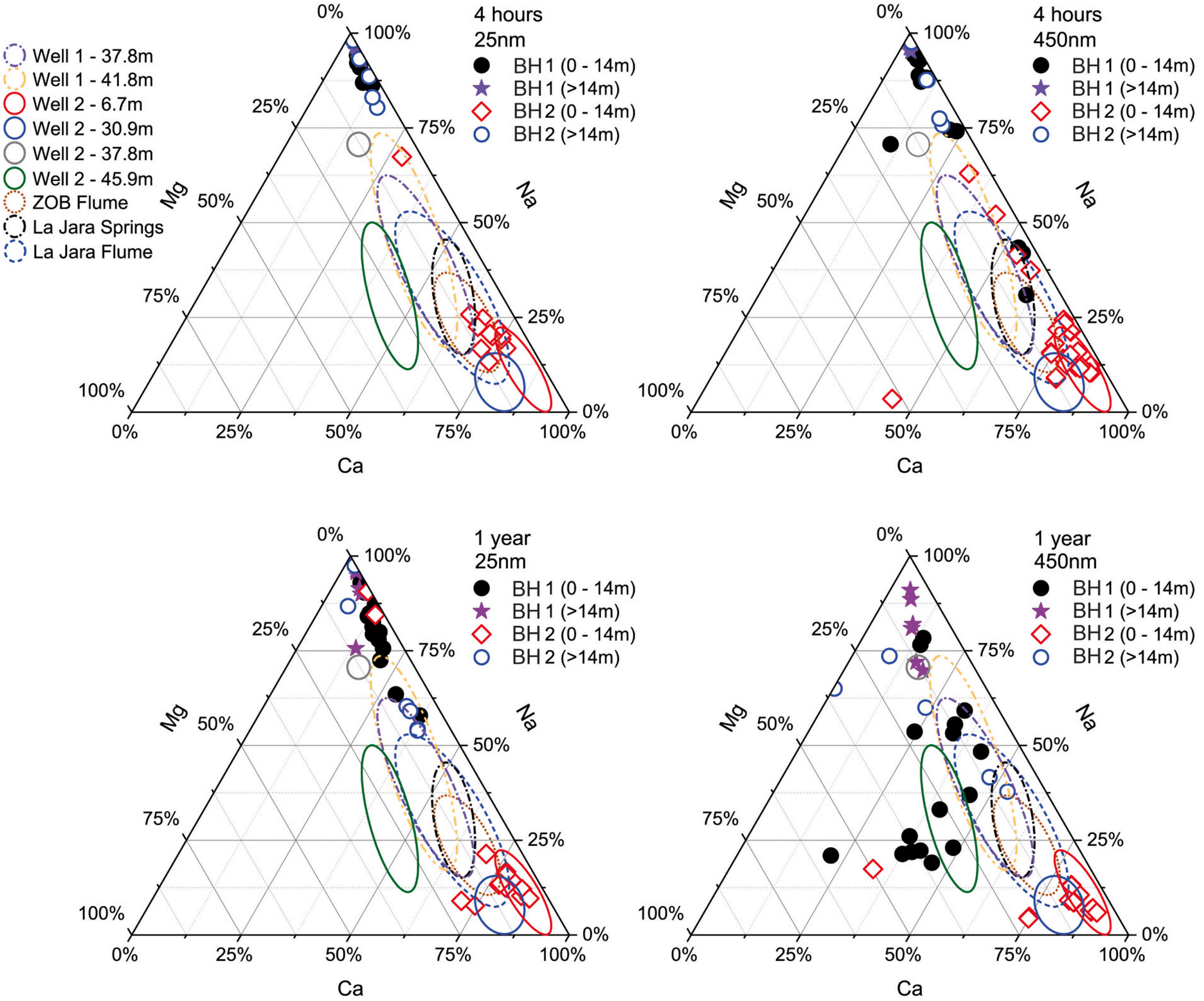

Fig. 11. Ternary diagrams of water Mg, Na, and Ca concentrations (in % meq) of spring, surface water, and groundwater samples (reported by White et al. (2019), filtered at 450 nm) for the ZOB and greater La Jara watershed compared to batch weathering samples for 4 h and 1 y. BH1 batch reaction samples, shown as closed symbols, correspond to Wells 1 (differentiated by maximum screen depth) and BH2 samples, open symbols, correspond with Wells 2 (differentiated by maximum screen depth). Field collected water chemistry data are shown with ellipses. Different filtrate sizes are shown for 4 h and 1-y batch reaction samples (see electronic version for color images).

5. Conclusions

Batch dissolution experiments were conducted with samples extracted from two continuous cores within the complex CZ architecture of a small, zero-order catchment in the Valles Caldera to understand depth- and time-discretized weathering processes and resulting water chemistry. Experimental results indicated that AT, with significant zeolite and smectite composition, were susceptible to weathering losses and colloidal dispersion. Initial colloidal dispersion subsequently exposed feldspars and zeolites to chemical attack by aggressive waters. Dispersed zeolites were subject to dissolution, and over the course of 1 y of weathering, dissolved products precipitated as colloidal smectite, incorporating Ca, Na, K, Mg, Mn, and some Fe into octahedral sheets and interlayer sites. We recognize that colloidal dispersion may have been promoted by the low solid to solution mass ratio employed (1:20 for this experiment), and future weathering experiments could vary this ratio to assess the timing for aqueous solutions to reach equilibrium and identify thresholds for colloidal dispersion.

Comparing both short- and long-term experimental weathering results to aqueous chemistry collected from the field point towards the utility of using a controlled experimental approach to elucidate chemical reactions responsible for observed water chemistry in the field, which informs our understanding of water routing and seasonal shifts in hydrologic flow paths. Aqueous solutions interacting with VB, comprised primarily of weathered lithics, were controlled by rapid calcite dissolution/precipitation reactions. Deep groundwater chemistry was controlled by disparate mechanisms. Water-rock interactions with deep, hydrothermally-altered VT had comparable chemical signatures to shallow AT. These chemical signatures (as aqueous base-cation proportions) were different from those in deep, unaltered, fracture-dominated T. We attribute these differences to available surface area susceptible to chemical attack by aggressive waters (greater in altered rocks) and primary mineral shielding from chemical attack by secondary Fe and Mn oxides and clay on fracture surfaces in unaltered T. We also attribute differences in water chemistry observed in deep monitoring wells in the fractured T compared to batch weathering reaction chemistry to unsaturated water-rock interactions in the AT in the near surface, which is rapidly mobilized downward during infiltration of snowmelt. A similar hydrochemical response in the deep CZ and fractured aquifers overlain by deeply weathered geologic material (particularly in volcaniclastic terrains) likely occurs in many other locations as fracture surfaces are often coated with secondary mineral phases at depth. This not only highlights the importance of understanding the connection between the shallow and deep CZ in terms of weathering and subsequent solution chemistry, but underscores a future direction in deep CZ science.

Experimental results also indicate the importance of defining what constitutes the dissolved fraction in aqueous solutions. Colloidal material can pass through 450 nm filter membranes (commonly defined operationally as the "dissolved fraction"), which can lead to overprediction of thermodynamic stability of primary and secondary aluminosilicates and Fe oxyhydroxides. Serial filtering of water samples, where aliquots from different filtrate sizes are collected and analyzed, provides direct evidence of colloidal contributions to landscape chemical denudation.

Supplementary data to this article can be found online at https://doi.org/10.1016/j.chemgeo.2020.119886.

Declaration of competing interest

The authors declare that they have no known competing financial interests or personal relationships that could have appeared to influence the work reported in this paper.

Acknowledgements

Funding for this project was provided by the National Science Foundation, grant no. EAR-1331408, in support of the Catalina-Jemez Critical Zone Observatory. Portions of this research were carried out at Stanford Synchrotron Radiation Laboratory, a National User Facility operated by Stanford University on behalf of the U.S. Department of Energy, Office of Basic Energy Sciences. Additional drilling, geophysical data, and core analysis and images may be accessed at http://osf.io/8fkzk. We thank Anders Noren and Ryan O'Grady from the Continental Scientific Drilling Coordination Office and LacCORE for their support on this project. We also wish to thank the filtering crew, MK Amistadi, R Burnett, D Carillo, K Orman, A McKenna, J Pelletier, R Gallery, A Sanchez, B Paras, Y Hu, S Pedron, N Abramson, M Pohlmann, R Dwivedi, D Fairbanks, and Cascade Drilling Inc. (Bothell, WA).

References

Bailey, R.A., Smith, R.L., Ross, C.S., 1969. Stratigraphic Nomenclature of Volcanic Rocks in the Jemez Mountains. New Mexico, US Geological Survey.

Bao, C., Li, L., Shi, Y.N., Duffy, C., 2017. Understanding watershed hydrogeochemistry: 1. Development of RT-Flux-PIHM. Water Resour. Res. 53 (3), 2328–2345.

Barker, W.W., Welch, S.A., Chu, S., Banfield, J.F., 1998. Experimental Observations of the Effects of Bacteria on Aluminosilicate Weathering. American Mineralogist, p. 1551.

Berg, A., Banwart, S.A., 2000. Carbon dioxide mediated dissolution of Ca-feldspar: implications for silicate weathering. Chem. Geol. 163 (1), 25–42.

Beria, H., Schaefli, B., Ceperley, N.C., Michelon, A., Larsen, J., 2017. How much of stream and groundwater comes from snow?. In: A Stable Isotope Perspective in the Swiss Alps, p. H44I-02.

Brantley, S.L., Olsen, A.A., 2014. Reaction kinetics of primary rock-forming minerals under ambient conditions. In: Holland, H.D., Turekian, K.K. (Eds.), Treatise on Geochemistry, Second edition. Elsevier, Oxford, pp. 69–113.

Brantley, S.L., White, A.F., 2009. Approaches to modeling weathered regolith. In: Oelkers, E.H., Schott, J. (Eds.), Thermodynamics and Kinetics of Water-Rock Interaction. Reviews in Mineralogy & Geochemistry, pp. 435–484.

Brooks, P.D., Vivoni, E.R., 2008. Mountain ecohydrology: quantifying the role of vegetation in the water balance of montane catchments. Ecohydrology 1 (3), 187–192.

Buss, H.L., Brantley, S.L., Scatena, F.N., Bazilievskaya, E.A., Blum, A., Schulz, M., Jiménez, R., White, A.F., Rother, G., Cole, D., 2013. Probing the deep critical zone beneath the Luquillo Experimental Forest, Puerto Rico. Earth Surf. Process Landf. 38 (10), 1170–1186.

Cadol, D., Galanter, A., Nicholls, P., 2015. Distribution and Transport of Pyrogenic Black Carbon in Soils Affected by Wildfires, Valles Caldera, New Mexico, with Implications for Contaminant Transport. New Mexico Water Resources Research Institute.

Casey, W.H., Bunker, B., 1990. Leaching of mineral and glass surfaces during dissolution. Rev. Mineral. 23, 397–426.

Casey, W.H., Westrich, H.R., Banfield, J.F., Ferruzzi, G., Arnold, G.W., 1993. Leaching and reconstruction at the surfaces of dissolving chain-silicate minerals. Nature 366 (6452), 253–256.

Chipera, S.J., Goff, F., Goff, C.J., Fittipaldo, M., 2008. Zeolitization of intracaldera sediments and rhyolitic rocks in the 1.25 Ma lake of Valles caldera, New Mexico, USA. J. Volcanol. Geotherm. Res. 178 (2), 317–330.

Chorover, J., et al., 2011. How water, carbon, and energy drive critical zone evolution: the Jemez-Santa Catalina critical zone observatory. Vadose Zone J. 10 (3), 884–899.

Cochand, M., Christe, P., Ornstein, P., Hunkeler, D., 2019. Groundwater storage in high alpine catchments and its contribution to streamflow. Water Resour. Res. 55 (4), 2613–2630.

Cole, J.W., Milner, D.M., Spinks, K.D., 2005. Calderas and caldera structures: a review. Earth Sci. Rev. 69 (1), 1–26.

Deer, W.A., 2013. An Introduction to the Rock-Forming Minerals. The Mineralogical Society, London.

Domanik, K., Kolar, S., Musselwhite, D., Drake, M.J., 2004. Accessory silicate mineral assemblages in the Bilanga diogenite: a petrographic study. Meteorit. Planet. Sci. 39 (4), 567–579.

Dorn, R.I., 2013. 4.5 rock coatings. In: Shroder, J.F. (Ed.), Treatise on Geomorphology. Academic Press, San Diego, pp. 70–97.

Drever, J.I., 1994. The effect of land plants on weathering rates of silicate minerals. Geochim. Cosmochim. Acta 58 (10), 2325–2332.

Drever, J.I., Stillings, L.L., 1997. The role of organic acids in mineral weathering. Colloids Surf. A Physicochem. Eng. Asp. 120 (1), 167–181.

Frazier, C.S., Graham, R.C., 2000. Pedogenic Transformation of Fractured Granitic Bedrock, Southern California. Soil Sci. Soc. Am. J. 64 (6), 2057–2069.

Goff, F., et al., 2011. Geologic Map of the Valles Caldera, Jemez Mountains, New Mexico, Geologic Map 79 (New Mexico Bureau of Geology and Mineral Resources).

Goldberg, S., 1989. Interaction of aluminum and iron oxides and clay minerals and their effect on soil physical properties: a review. Commun. Soil Sci. Plant Anal. 20 (11−12), 1181–1207.

Graham, R.C., Herbert, B.E., Ervin, J.O., 1988. Mineralogy and incipient pedogenesis of entisols in anorthosite terrane of the San Gabriel Mountains, California. Soil Sci. Soc. Am. J. 52 (3), 738–746.

Guo, L., Santschi, P., 2007. Ultrafiltration and Its Applications to Sampling and Characterisation of Aquatic Colloids, pp. 159–221.

Hasenmueller, E.A., Gu, X., Weitzman, J.N., Adams, T.S., Stinchcomb, G.E., Eissenstat, D. M., Drohan, P.J., Brantley, S.L., Kaye, J.P., 2017. Weathering of rock to regolith: The activity of deep roots in bedrock fractures. Geoderma 300, 11–31.

Hayes, S.M., Root, R.A., Perdrial, N., Maier, R.M., Chorover, J., 2014. Surficial weathering of iron sulfide mine tailings under semi-arid climate. Geochim. Cosmochim. Acta 141, 240–257.

Henderson, J.H., 1971. Cristobalite authigenic origin in relation to montmorillonite and quartz origin in bentonites. Clays and Clay Minerals 19 (4), 229− +.

Hoagland, B., et al., 2017. Hyporheic zone influences on concentration-discharge relationships in a headwater sandstone stream. Water Resour. Res. 53 (6), 4643–4667.

Holbrook, W.S., et al., 2019. Links between physical and chemical weathering inferred from a 65-m-deep borehole through Earth's critical zone. Sci. Rep. 9 (1), 4495.

Hulen, J.B., Nielson, D.L., 1986. Hydrothermal alteration in the Baca Geothermal System, Redondo Dome, Valles Caldera, New-Mexico. J. Geophys. Res. Solid Earth Planets 91 (B2), 1867–1886.

Hulen, J.B., Nielson, D.L., 1988. Hydrothermal brecciation in the Jemez Fault Zone, Valles Caldera, New-Mexico - results from Continental Scientific Drilling Program Core Hole VC-1. J. Geophys. Res. Solid Earth Planets 93 (B6), 6077–6089.

Hulen, J.B., Nielson, D.L., 1991. Evolution of the Western Valles Caldera complex, New-Mexico - evidence from intracaldera sandstones, breccias, and surge deposits. J. Geophys. Res. Solid Earth Planets 96 (B5), 8127–8142.

Hunsaker, C.T., Johnson, D.W., 2017. Concentration-discharge relationships in headwater streams of the Sierra Nevada, California. Water Resour. Res. 53 (9), 7869–7884.

Ibarra, D.E., et al., 2016. Differential weathering of basaltic and granitic catchments from concentration-discharge relationships. Geochim. Cosmochim. Acta 190, 265–293.

Ilavsky, J., 2012. Nika: software for two-dimensional data reduction. J. Appl. Crystallogr. 45, 324–328.

Izett, G.A., Obradovich, J.D., 1994. Ar-40/Ar-39 Age constraintes for the Jaramillo normal subchron and the Matuyama-Brunhes geomagnetic boundary. Journal of Geophysical Research-Solid Earth 99 (B2), 2925–2934.

Jenicek, M., Ledvinka, O., 2020. Importance of snowmelt contribution to seasonal runoff and summer low flows in Czechia. Hydrol. Earth Syst. Sci. 24 (7), 3475–3491.

Jin, L.X., et al., 2010. Mineral weathering and elemental transport during hillslope evolution at the Susquehanna/Shale Hills Critical Zone Observatory. Geochim. Cosmochim. Acta 74 (13), 3669–3691.

Kim, H., Dietrich, W.E., Thurnhoffer, B.M., Bishop, J.K.B., Fung, I.Y., 2017. Controls on solute concentration-discharge relationships revealed by simultaneous hydrochemistry observations of hillslope runoff and stream flow: the importance of critical zone structure. Water Resour. Res. 53 (2), 1424–1443.

Kim, J.G., Lee, G.H., Lee, J.S., Chon, C.M., Kim, T.H., Ha, K., 2006. Infiltration pattern in a regolith-fractured bedrock profile: field observation of a dye stain pattern. Hydrol. Process. 20 (2), 241–250.

Lee, M.R., Hodson, M.E., Parsons, I., 1998. The role of intragranular microtextures and microstructures in chemical and mechanical weathering: direct comparisons of experimentally and naturally weathered alkali feldspars. Geochim. Cosmochim. Acta 62 (16), 2771–2788.

Li, L., et al., 2017. Expanding the role of reactive transport models in critical zone processes. Earth Sci. Rev. 165, 280–301.

Malmström, M.E., Destouni, G., Banwart, S.A., Strömberg, B.H.E., 2000. Resolving the scale-dependence of mineral weathering rates. Environmental Science & Technology 34 (7), 1375–1378.

McGlynn, B.L., McDonnell, J.J., Seibert, J., Kendall, C., 2004. Scale effects on headwater catchment runoff timing, flow sources, and groundwater-streamflow relations. Water Resour. Res. 40 (7).

McIntosh, J.C., et al., 2017. Geochemical evolution of the critical zone across variable time scales informs concentration-discharge relationships: Jemez River Basin Critical Zone Observatory. Water Resour. Res. 53 (5), 4169–4196.

Moravec, B.G., et al., 2020. Resolving deep critical zone architecture in complex volcanic terrain. Journal of Geophysical Research: Earth Surface 125 (1), e2019JF005189.

Navarre-Sitchler, A., Brantley, S., 2007. Basalt weathering across scales. Earth Planet. Sci. Lett. 261 (1–2), 321–334.

Navarre-Sitchler, A., Brantley, S.L., Rother, G., 2015. How porosity increases during incipient weathering of crystalline silicate rocks. In: Steefel, C.I., Emmanuel, S., Anovitz, L.M. (Eds.), Pore-Scale Geochemical Processes. Reviews in Mineralogy & Geochemistry, pp. 331–354.

Ockenden, M.C., et al., 2016. Changing climate and nutrient transfers: evidence from high temporal resolution concentration-flow dynamics in headwater catchments. Sci. Total Environ. 548-549, 325–339.

Olshansky, Y., White, A.M., Moravec, B., McIntosh, J., Chorover, J., 2018. Subsurface pore water contributions to stream concentration-discharge relations across a snowmelt hydrograph. Front. Earth Sci. 6.

Parkhurst, D.L., Appelo, C.A.J., 1999. User's Guide to PHREEQC (Version 2) : a Computer Program for Speciation, Batch-Reaction, One-Dimensional Transport, and Inverse Geochemical Calculations, pp. 99–4259.

Phillips, E.H., et al., 2007. The Ar-40/Ar-39 age constraints on the duration of resurgence at the Valles caldera, New Mexico. Journal of Geophysical Research-Solid Earth 112 (B8).

Pohlmann, M., et al., 2016. Pore water chemistry reveals gradients in mineral transformation across a model basaltic hillslope. Geochemistry Geophysics Geosystems 17 (6), 2054–2069.

Rasmussen, C., et al., 2011. Strong climate and tectonic control on plagioclase weathering in granitic terrain. Earth Planet. Sci. Lett. 301 (3–4), 521–530.

Schulze, D.G., 1981. Identification of soil iron-oxide minerals by differential x-ray diffraction. Soil Sci. Soc. Am. J. 45 (2), 437–440.

Smith, R.L., Bailey, R.A., 1966. The Bandelier Tuff: a study of ash-flow eruption cycles from zoned Magma Chambers. Bull. Volcanol. 29 (1), 83–103.

Sparks, D.L., 2003. Environmental Soil Chemistry. Academic Press, Amsterdam.

Spell, T.L., McDougall, I., Doulgeris, A.P., 1996. Cerro Toledo Rhyolite, Jemez Volcanic Field, New Mexico: Ar-40/Ar-39 geochronology of eruptions between two caldera-forming events. Geol. Soc. Am. Bull. 108 (12), 1549–1566.

Tague, C., Grant, G.E., 2009. Groundwater dynamics mediate low-flow response to global warming in snow-dominated alpine regions. Water Resources Research 45.

Trostle, K.D., et al., 2016. Colloids and organic matter complexation control trace metal concentration-discharge relationships in Marshall Gulch stream waters. Water Resour. Res. 52 (10), 7931–7944.

van Grinsven, J.J.M., van Riemsdijk, W.H., 1992. Evaluation of batch and column techniques to measure weathering rates in soils. Geoderma 52 (1), 41–57.

Vazquez-Ortega, A., et al., 2015. Rare earth elements as reactive tracers of biogeochemical weathering in forested rhyolitic terrain. Chem. Geol. 391, 19–32.

Weaver, C.E., 1978. Mn-Fe coatings on saprolite fracture surfaces. J. Sediment. Petrol. 48 (2), 595–610.

White, A., Buss, H., 2013. Natural Weathering Rates of Silicate Minerals, pp. 115–155.

White, A.F., et al., 2001. Differential rates of feldspar weathering in granitic regoliths. Geochim. Cosmochim. Acta 65 (6), 847–869.

White, A., et al., 2019. Distinct stores and the routing of water in the deep critical zone of a snow-dominated volcanic catchment. Hydrol. Earth Syst. Sci. 23 (11), 4661–4683.

Whittig, L.D., Allardice, W.R., 1986. X-ray diffraction techniques. In: Klute, A. (Ed.), Methods of Soil Analysis, Part 1: Physical and Mineralogical Methods. American Society of Agronomy, Madison, pp. 331–362.

Wolff, J.A., Gardner, J.N., 1995. Is the Valles Caldera entering a new cycle of activity. Geology 23 (5), 411–414.

Zapata-Rios, X., et al., 2015. Climatic and landscape controls on water transit times and silicate mineral weathering in the critical zone. Water Resour. Res. 51 (8), 6036–6051.